Biophysical *Journal*
Article

Biophysical Society

Disentangling cadherin-mediated cell-cell interactions in collective cancer cell migration

Themistoklis Zisis,[1,6] David B. Brückner,[2,3,6] Tom Brandstätter,[2] Wei Xiong Siow,[1] Joseph d'Alessandro,[4] Angelika M. Vollmar,[1] Chase P. Broedersz,[2,5,*] and Stefan Zahler[1,*]

[1]Ludwig-Maximilians-University Munich, Department of Pharmacy, Center for Drug Research, Munich, Germany; [2]Arnold Sommerfeld Center for Theoretical Physics and Center for NanoScience, Department of Physics, Ludwig-Maximilians-University Munich, Munich, Germany; [3]Institute of Science and Technology Austria, Klosterneuburg, Austria; [4]Institut Jacques Monod (IJM), CNRS UMR 7592 and Université de Paris, Paris, France; and [5]Department of Physics and Astronomy, Vrije Universiteit Amsterdam, Amsterdam, the Netherlands

ABSTRACT Cell dispersion from a confined area is fundamental in a number of biological processes, including cancer metastasis. To date, a quantitative understanding of the interplay of single-cell motility, cell proliferation, and intercellular contacts remains elusive. In particular, the role of E- and N-cadherin junctions, central components of intercellular contacts, is still controversial. Combining theoretical modeling with in vitro observations, we investigate the collective spreading behavior of colonies of human cancer cells (T24). The spreading of these colonies is driven by stochastic single-cell migration with frequent transient cell-cell contacts. We find that inhibition of E- and N-cadherin junctions decreases colony spreading and average spreading velocities, without affecting the strength of correlations in spreading velocities of neighboring cells. Based on a biophysical simulation model for cell migration, we show that the behavioral changes upon disruption of these junctions can be explained by reduced repulsive excluded volume interactions between cells. This suggests that in cancer cell migration, cadherin-based intercellular contacts sharpen cell boundaries leading to repulsive rather than cohesive interactions between cells, thereby promoting efficient cell spreading during collective migration.

SIGNIFICANCE Collective cell migration from restricted areas is an essential part of many physiological and disease-associated biological phenomena. In these processes, cell organize their collective behavior through cell-cell contacts, which include E- and N-cadherin-mediated interactions. Yet, the distinct effects of these contacts on collective migration remain poorly understood. Here, we show that both cadherin junction types enhance the spreading efficiency of cancer cell clusters by promoting repulsive excluded-volume interactions between cells. This unexpected finding highlights intercellular repulsion as a decisive player in collective cell migration and underscores the importance of cadherins as potential pharmacological targets.

INTRODUCTION

Collective cell migration is central to a number of key physiological processes, including morphogenesis during development (1), as well as immune response (2), wound repair (3), and tissue homeostasis (4) in the developed organism. Aberrant cell migration is associated with several pathologies, such as the spread of malignant cancer cells to previously healthy tissues during metastasis (5). The migratory dynamics of cell collectives in these processes are not merely the outcome of many independently moving cells: they are controlled by cell-cell interactions (6,7). Specifically, cells form mechanosensitive cell-cell adhesion junctions (adherens junctions) and coordinate their movements by actively interacting with each other (8). These interactions facilitate a coordination of collective behavior where a colony of cells invades an empty area (9). However, it remains unclear how different types of cell-cell interactions control such collective spreading behavior.

The trajectories of single migrating cells are well described by stochastic trajectory models, both for cells migrating on two-dimensional (2D) surfaces (10–12) and in confining environments (13–16). Yet, it is challenging to describe the stochastic collective migration of a cancer

Submitted March 29, 2021, and accepted for publication December 6, 2021.

[6]These authors contributed equally

*Correspondence: stefan.zahler@cup.uni-muenchen.de or c.broedersz@lmu.de

Editor: Celeste Nelson.

https://doi.org/10.1016/j.bpj.2021.12.006

cell colony, as cell division and cell-cell contacts have to be taken into consideration. Cell-cell contacts lead to a variety of interactions between cells. First, cells exhibit excluded volume (EV) interactions, where an individual cell occupies space and exerts a repelling force on other cells that move within this space (17). Second, many cell types have the tendency to reorient their direction of motion and move apart upon contact, which is referred to as contact inhibition of locomotion (CIL) (18,19). In physical stochastic trajectory models, these interactions are frequently incorporated as a combination of "repulsive interactions," modeling EV, and "velocity interactions," including velocity alignment as well as CIL (20–24). Conceptually, there is a key difference between these interactions: although repulsive interactions depend on the relative positions of cells, velocity interactions depend on their motion, i.e., their velocities or polarities. However, it remains unclear how changes in cell-cell contacts within a migrating colony influence these distinct types of interactions and the resulting collective migratory behavior.

Intercellular interactions are strongly dependent on cadherins, highly conserved calcium-dependent transmembrane proteins that constitute the main component of adherens junctions. Type I classical cadherins (including epithelial (E) and neuronal (N) cadherin as well as P-, R- and M-cadherin (25)) form strong cell-cell adhesion by predominantly homotypic interaction between their extracellular domains (26). The intracellular cadherin domains connect to β- and α-catenins that associate with the actin cytoskeleton to mediate mechanotransduction (27). Changes in the normal expression levels of the different cadherin types has been associated with carcinogenesis. One of the most studied processes related to several epithelial tumors is the cadherin switch observed during epithelial-mesenchymal transition (EMT). EMT involves the loss of epithelial cell polarity and cell-cell adhesion and the gain of migratory and invasive properties, resulting in the predominance of a mesenchymal phenotype (28). More specifically, there typically is a strong downregulation of E-cadherin in parallel with an upregulation of N-cadherin in EMT. As a result, E-cadherin adherens junctions disassociate while N-cadherin junctions establish a relatively weak (compared with E-cadherin) adherens junction (29).

However, the role of E- or N-cadherin-mediated intercellular adhesions in cancer cell migration remains controversial. On the one hand, E-cadherin downregulation has been related to cancer development (30,31), and it has been shown that the presence of E-cadherin induces a spreading cell monolayer to retract and form a spheroid aggregate, a process called dewetting (32), suggesting its role as a potent tumor suppressor. On the other hand, a number of studies suggest the opposite effect: E-cadherin is required for coordinated collective movement of cancer cells in organotypic culture (33) and for metastasis in multiple models of breast cancer (34); it promotes expansion of bladder carcinoma in situ (35); and is highly present in patients with prostate cancer (36), ovarian cancer (37), and glioblastoma (38). A similar controversy characterizes the involvement of N-cadherin in migratory behavior. Although N-cadherin is a marker of EMT and its expression has been associated with the development of multiple cancer types (29), there are studies pointing in the opposite direction. In fact, N-cadherin loss was associated with increased tumor incidence (39) and metastasis (40). Consequently, a question is yet to be answered: what is the distinct contribution of E- and N-cadherin junctions to cell-cell interactions and the resulting spreading dynamics of cancer cell colonies?

Here, we aim to investigate this question by combining experimental observations on collectively migrating cells and a minimal physical model of the spreading behavior. We use an epithelial bladder cancerous cell line (T24), which is characterized by high N-cadherin expression and limited (41) or zero functional levels of E-cadherin (42,43). After initial confinement of a colony of cells to a circular micropattern, the cells are released using chemical tools (44,45). We quantify the collective migration by identifying and tracking the entire ensemble of single-cell trajectories in each colony. To investigate the effect of cell-cell contacts for the migration, we inhibit E- or N-cadherin junctions via specific blocking antibodies. In both cases, our analysis reveals that such inhibition leads to a reduced spreading velocity of the cell colonies. To elucidate these dynamics, we develop a minimal active particle model for collective migration, that includes cell proliferation as well as repulsive and CIL interactions. This model shows that inhibiting E- or N-cadherin has an effect akin to reducing the strength of repulsive cell-cell interactions in the model. In other words, disturbing either of these cadherin junctions decreases the displacement generated when neighboring cells push each other away in order to create space for themselves. Therefore, we show that both E- and N-cadherins contribute to the maintenance of intercellular contacts that facilitate cell spreading via repulsive interactions, causing cells to move farther away from each other. This could be a consequence of cadherins "sharpening" cellular boundaries, through, e.g., shape regulation, changes in interfacial tension, or increased cell-cell recognition (46). These observations indicate the important role of cadherins in metastatic events and their potential as cancer treatment targets.

MATERIALS AND METHODS

T24 cell culture transfection with H2B-GFP plasmid for nucleus labeling

H2B-GFP expression vectors were obtained from Addgene (#11680; Watertown, MA). T24 cells exponentially growing in Dulbecco's modified Eagle's medium (DMEM) supplemented with 10% fetal calf serum (FCS) were transfected with 2.5 μg of the H2B-GFP expression vector carrying a G418 resistance as selection marker, using an Amaxa (Colgne,

Germany) R-Kit (Program I-013) under constant humidity at 37°C and 5% CO_2. Twenty-four hours after the transfection, cells were treated with G418 (A1720; Sigma-Aldrich, St. Louis, MO) to an end concentration of 0.8 mg/mL in 2-mL well-plates and then further cultivated in T25 flasks and later on in T75 flasks with the same concentration of G418 (0.8 mg/mL). After two rounds of additional cell sorting by flow cytometry the GFP+ cells at passage 30 were frozen in a nitrogen tank at a concentration of 1×10^6 cells/mL.

For all collective migration experiments, T24 cells were pregrown as monolayers and diluted down to the desired concentrations in DMEM supplemented with 10% FCS, 10.000 U/mL penicillin/streptomycin, and 0.8 mg/mL antibiotic G418 under constant humidity at 37°C and 5% CO_2.

Microcontact printing for circular pattern generation

Eight-well uncoated μ-Slides (ibidi, Martinsried, Germany) underwent 3 min of oxygen plasma treatment (Plasma cleaner type "ZEPTO," Diener electronic, Ebhausen, Germany) at 0.3 mbar for activation (generation of OH-hydroxyl bonds). Then, 250 μL/well of 0.05 mg/mL fibronectin (R&D Systems, Minneapolis, MN) solution in MilliQ were added to the now highly reactive surface and incubated at room temp for 2 h. After washing 2 times with 500 μL of milliQ H_2O, the surface was allowed to dry. Following that, we used standard microcontact printing techniques to create PDMS stamps with circular patterns. We placed one stamp at the center of each well and plasma-treated the surface one last time at the same conditions as before. This step removes all fibronectin from the surface except the areas that are protected by the stamp, so all the unprotected areas on the surface become hydroxylated and highly reactive again. Without removing the stamps, we added a 7-μL drop of 1 mg/mL PLL(20)-g[3.5]-PEG-N_3(3) (APP) (Susos AG, Dubendorf, Switzerland) solution in MilliQ right next to each stamp allowing surface tension to absorb the liquid underneath the stamp. We let the preceding condition settle for 45 min. We gently removed the stamp and washed two times with 500 μL of MilliQ. Now the circular areas contain fibronectin and are highly cell-adhesive while the surrounding areas are initially cell repellent. At this point, T24 cells were trypsinized after reaching confluency, diluted to the desired density (70,000 cells/mL) in the aforementioned DMEM-based medium, and 250 μL of this cell suspension was added in each well and allowed to settle overnight at 37°C. The next day, the cell medium was replaced with 200 μL of fresh medium and the slide was placed under the microscope. Finally, 10 μL of 100μM BCN-cRGDfk (Synaffix, Amsterdam, The Netherlands) in phosphate-buffered saline (PBS) was added in the medium of each well to a final concentration of 20 μM. The BCN groups formed a link with the azide groups of the APP-covered, cell-repellent areas around the colonies. This resulted in the binding of RGD on the surface, thereby rendering the surrounding areas cell-adhesive and initiating cell migration.

Blocking antibody treatment of T24 circular colonies

For the blocking antibody treatment experiments, we followed the exact same cell preparation protocol as described previously with the addition of the following steps: On the next day, after the first washing step, 200 μL of 5 mM EGTA solution was added in each well for 30 min. This step was performed to break the existing cadherin junctions and allow the blocking antibodies (anti N-cadherin antibody: LEAF Purified anti-human CD325, #350804, BioLegend, San Diego, CA; anti E-cadherin antibody: CD324 #16-3249-82, Invitrogen, Carlsbad, CA) to bind to their respective epitopes. Following that, the wells were washed two times with 200 μL of fresh cell medium. Subsequently, 200 μL of the appropriate E- (10 or 25μg/mL) or N-cadherin (25, 50, or 100μg/mL) blocking antibody solution in cell medium was added in each well. Cells were incubated additionally for 30 min and then the slide was placed under the microscope. Finally, 10 μL of 100μM BCN-cRGDfk (Synaffix) in PBS was added to the medium of each well to a final concentration of 20 μM.

Cell imaging

Live cell imaging was performed using the T24 seeded 8-well fibronectin/APP patterned slides with an Eclipse Ti inverted microscope (Nikon, Dusseldorf, Germany) with a ×4/×10 phase contrast objective and a charge-coupled device camera (DS-Qi1Mc; Nikon). The slides were inserted into a 37°C heating and incubation system that was flushed with actively mixed 5% CO_2 at a rate of 10 L/h, and the humidity was kept at 80% to prevent dehydration. The cells were imaged in bright-field and the fluorescence of the nuclei was detected at a 488-nm wavelength using the integrated fluorescence LED. Time-lapse video microscopy was performed with a time interval of 5 min between images over 24 h.

Evaluation of cell division

Using the videos acquired as described previously, we manually tracked the number of cell divisions in each frame in the outer ring (edge) versus the inner area (core) of the cluster; the definition of these areas can be observed in Fig. S8. For each area, the number of cell divisions counted was divided by the total number of cells in that area and expressed as a percentage of the total cell divisions.

Tracking of single-cell trajectories

The positions of individual cells were detected as previously described (45) using custom-made ImageJ (National Institutes of Health, Bethesda, MD) macros implementing the "Find Maxima" built-in function. The individual trajectories were then reconstructed using a squared-displacement minimization algorithm (http://site.physics.georgetown.edu/matlab) and data analysis was performed via custom-made MATLAB programs (MathWorks, Natick, MA).

Quantitative polymerase chain reaction

T24 cells were lysed for messenger RNA (mRNA) isolation. Briefly, "Buffer RLT, Lysis Buffer" (RNeasy Mini Kit (250) PCR lab; QIAGEN, Hilden, Germany) was mixed with DTT 2M at a ratio of 50:1. After medium aspiration and ice-cold PBS rinsing, ice-cold lysis buffer was added and the lysates were stored at −80°C. For the mRNA, isolation the RNeasy Mini Kit (250) (QIAGEN) was used according to the modified manufacturer's instructions; 2 μL of the mRNA samples was used directly for mRNA concentration determination using a Nanodrop Spectrophotometer (PEQLAB Biotechnologie, Erlangen, Germany) with absorption at 260 nm (specific for mRNA) while impurities were determined at 280 nm. For the reverse transcription of mRNA to complementary DNA (cDNA), 2X RT master mix was prepared containing 10% TaqMan RT Puffer-10x, 0.04% dNTPs, 10% random hexamers, 5% reverse transcriptase, 21%RNAase free water, 50% H_2O + RNA 2.5 μg. For the quantitative PCR (qPCR), the following primers were obtained from metabion GmbH (Planegg, Germany): E-Cadh_1_F (MM125, 5′TGGG CCAGGAAATCACATCC-3′), E-Cadh_1_R (MM126, 5′GGCACCAGT GTCCGGATTAA-3′); N-Cadh_2_F (MM133, 5′CCTTTCAAACACAGCC ACGG-3′), N-Cadh_2_R (MM134, 5′TGTTTGGGTCGGTCTGGATG-3′). We used 2 μL of the acquired cDNA in each well of the MicroAmp Fast Optical 96-Well Reaction Plate or 2 μL of autoclaved Millipore (Bedford, MA) H_2O for the no-template controls, respectively; 10.5 μL of PCR master mix containing 6.25 μL of PowerUPTM SYBR Green Master Mix, 3.75 μL of autoclaved Millipore H_2O, 0.25 μL of forward primer, and 0.25 μL of reverse primer were added to each probe well and the qPCR was performed in a QuantStudio 3 Real-Time PCR system (ThermoFisher, Waltham, MA). Data were normalized to the housekeeping gene GAPDH. The analysis was carried out with the

ΔΔCT method as previously described (47), using the ThermoFisher cloud, and threshold cycle was set to >9 to 15 and ≤30 to allow acceptable detection for best reproducibility.

Western blots

Cells were harvested and lysed in RIPA lysis buffer containing a protease inhibitor mix (#4693159001; Roche, Basel, Switzerland). Lysates were centrifuged at 10,000 × *g* for 10 min and 4°C. Protein amounts were assessed by Bradford assay, and an equal amount of protein was separated by sodium dodecyl sulfate-polyacrylamide gel electrophoresis and transferred to nitrocellulose membranes (Hybond-ECLTM; Amersham Bioscience, Little Chalfont, UK). Membranes were incubated with blocking buffer containing 5% bovine serum albumin (BSA) and 0.1% Tween 20 in PBS for 1 h at room temperature, followed by 3 × 5 min rinsing with PBS-T. After that, membranes were incubated with rabbit anti-ECAD (24E10) monoclonal Ab (1:500; #3195, Cell Signaling Technology, Inc. USA) or rabbit anti-NCAD (D4R1H) XP monoclonal Ab (1:500; #13116, Cell Signaling Technology Inc., Danvers, MA) at 4°C overnight. Membranes were washed again with PBS-T three times for 5 min. Secondary antibody (horseradish peroxidase-goat-anti-rabbit 1:1000; #111-035-144, Dianova, Hamburg, Germany) was used for 2-h incubation at room temperature and subsequently conjugated with horseradish peroxidase and freshly prepared ECL solution (protected from light), which contained 2.5 mM luminol (detailed description of ECL solution preparation in Table 1). Conjugated proteins were detected by the ChemiDoc Touch Imaging System (Bio-Rad, Hercules, CA) and quantified by ImageLab software (Bio-Rad). For quantification, protein amount was normalized to total protein loading, detected by 2,2,2-trichloroethanol activation as described previously (47,48).

Immunohistochemistry

We performed the following stainings

- E-cadherin + N-cadherin + Hoechst co-staining (Methanol/acetone fixation protocol)
- γ-Tubulin + Actin + Hoechst co-staining (Methanol/acetone fixation protocol)
- γ-Tubulin + Hoechst co-staining (Methanol/acetone fixation protocol)
- Actin + Hoechst co-staining (PFA fixation protocol)

Cells were fixed at 5 h or 24 h after the start of cell migration with 4% PFA (only in case of actin staining) or 1:1 pure methanol/acetone for 20 min. After 10 min of permeabilization with 250 μL/well 0.5% Triton X-100 at room temperature (only for actin staining) and 5 × 5-min washings with PBS, cells were incubated with (1% BSA in PBS, 250 μL/well) at room temperature for 1 h. Then the primary antibody was added (150 μL/well). The details on the primary antibodies used are listed in Table 2.

After overnight incubation with the primary antibody, the solution was removed and cells were washed five times for 5 min with PBS and then incubated with secondary antibody in 1% BSA for 1 h at room temperature in the dark. The details on the secondary antibodies used are listed in Table 3.

The solution was then removed and cells were washed five times for 5 min with PBS. For mounting, 1 drop of mounting medium was added before sealing with cover slips and Incubating for 30 min at room temperature.

TABLE 1 Western blot reagents

#	Reagent	Volume, μL	Stock
1	distilled Water	4500	
2	Tris-Base pH 8.5	500	
3	p-coumaric acid	22	15 mg/mL in dimethyl sulfoxide (DMSO) (Aliquots at −20°C)
4	Luminol	50	44 mg/mL in DMSO (Aliquots at −20°C)
5	H2O2 30%	3	

TABLE 2 Primary antibodies

Target	Company	Lot	Dilution	Species	Number
Ecad	Invitrogen	131,700	1:2000	Mouse	531
Ncad	Cell signaling	4016	1:200	Rabbit	477
γ-Tubulin	Sigma	T 6557	1:200	Mouse	380

Imaging and image analysis of stainings

Cells were imaged using a Leica TCS SP8 confocal microscope with HC PL Fluotar CS2 10×/0.3 NA DRY (Leica, Wetzlar, Germany) using LAS X Core software. For the imaging of E- and N- cadherin, γ-Tubulin, and actin staining, the argon laser with an excitation wavelength of 488 or 647 nm was used, and the wavelength range of the detector was set between 480 and 530 and 640 and 680 nm, respectively. For Hoechst 33,342 imaging, the diode laser was employed with excitation wavelength of 405 nm and the detection wavelength was set between 460 and 490 nm. All images were analyzed using the ImageJ version 1.53c61 software tool.

For the assessment of cell polarization on the γ-Tubulin (+actin) + Hoechst costained colonies, we consider a cell to be polarized when the microtubule-organizing center (MTOC; visible as a distinguished green dot) is located rear/frontal to the nucleus in relation to the direction of movement (49). The direction of movement is toward the higher microtubule distribution edge in each cell (50). We quantified the number of cells polarized away from cell-cell contacts (examples in red arrows), toward cell-cell contacts (examples in blue arrows) or nonpolarized (orange arrows) at the edge of the cluster (Fig. S7). The numbers were divided by the total number of counted cells at the edge of the cluster.

For the analysis of E- and N-cadherin immunofluorescence in untreated (control) colonies versus E- or N-cadherin blocking antibody-treated colonies, we measured the fluorescence intensity in each channel (green for E-cadherin and red for N-cadherin). The fluorescence intensity of each the blocking condition was normalized to the fluorescence intensity of the control condition.

Cross-correlation functions of velocity fluctuations

To investigate the interactions of cells in the experiment, we calculated the spatial velocity cross-correlation function

TABLE 3 Secondary antibodies and other staining reagents

2nd Antibody/dye	Company	Lot	Dilution	Species/specificity
Alexa Fluor 488-Ab“ (for gamma Tubulin and E-cadherin)	Invitrogen	11,001	1:400	Goat anti-mouse
Alexa Fluor 647-Ab “(for N-cadherin)	Invitrogen	21,443	1:400	Chicken anti-rabbit
Hoechst 33,342 (blue-fluorescent)	Thermo Scientific	62,249	1:400	Nuclear-specific dye
Actin stain (red-fluorescent phalloidin)	Invitrogen	22,287	1:400	Specific to native quaternary structure of F-actin

$$C(r) = \frac{\sum_{ij} v_i \cdot v_j \delta(r - r_{ij})}{\sum_{ij} \delta(r - r_{ij})},$$

where v_i is the 2D velocity vector of cell i and $\delta(r - r_{ij})$ is the Dirac delta-function. This function measures how "similar" the velocities (magnitude and direction) of cells at distance r from one another are on average. Using discrete bins as an approximation for the delta-function for finite data, we obtain expected results both for experimental and simulated data.

The complete velocity field is composed of the collective outward motion, a dilatational mode, and additional velocity fluctuations due to interactions between the cells. Following previous work (51), we calculated these fluctuations by obtaining the scalar dilatation D as a function of time, by optimizing the quantity $\sum_i [x_i(t+T) - Dx_i(t)]^2$. The fluctuation velocities are then giving by $u_i = [x_i(t+T) - Dx_i(t)]/T$. Note that here, we use a time interval $T = 15\Delta t$, which is larger than the time-resolution of the experiment. This allows us to average out the short time-scale noise fluctuations of the cellular velocities, and instead focusses on longer time-scale process relevant to the spreading dynamics. We test this approach in our simulations, and find that it accurately detects the presence of velocity-dependent interactions, such as CIL (Fig. S4).

Dilatational order parameter

To estimate the order parameter of the collective spreading process, we calculated the dilatational order parameter Λ, as previously defined in (51):

$$\Lambda = \sum_i \frac{x_i(t) \cdot [x_i(t+T) - x_i(t)]}{|x_i(t)||[x_i(t+T) - x_i(t)]|},$$

using $T = \Delta t$. This parameter is defined in the range $-1 < \Lambda < 1$, and measures the degree of coherent expansion (for $\Lambda > 0$) or contraction (for $\Lambda < 0$). For Λ close to 0, there is little dilatational order.

Computational modeling

To provide a minimal computational model for the spreading process, we implement a simple active particle model for collective cell migration. Similar to previous works (22,45,52–55), we describe the motion of the cells using stochastic equations of motion with interactions. Specifically, we use the equation of motion

$$\frac{d\vec{v}_i}{dt} = -\gamma \vec{v}_i + \vec{F}_{\text{rep}}(|r_i - r_j|) + \vec{F}^i{}_{\text{CIL}} + \sigma \vec{\eta}_i(t),$$

where $\vec{\eta}_i(t)$ represents a Gaussian white noise with $\langle \vec{\eta}_i(t) \rangle = 0$ and $\langle \vec{\eta}_i(t) \vec{\eta}_j(t') \rangle = \delta(t - t')\delta_{ij}$. The model furthermore includes a persistence term $-\gamma v$, where γ^{-1} is the persistence time of the cells. The repulsive interactions are implemented as the repulsive part of a quadratic potential

$$\vec{F}_{\text{rep}} = -\varepsilon(2\lambda - r_{ij}) \frac{\vec{r}_{ij}}{r_{ij}},$$

where λ represents the radius of the cells, and ε is the strength of the interaction.

The CIL interaction $\vec{F}_{\text{CIL}}$ is implemented in the form of a rotation of the velocity vector away from the distance vector $\vec{r}_{ij} = \vec{r}_j - \vec{r}_i$ to nearest neighbors, which are defined by being within an interaction range of radius 2.5λ, and being on collision course with cell i, i.e., $\vec{v}_i \cdot \vec{r}_{ij} > 0$. The angular displacement only depends on the velocity direction, a constant acceleration α, and the number as well as the positions of nearest neighbors: For each nearest neighbor, the direction of the axis of rotation is found such that the rotation will be away from the nearest neighbors. All directions of the axes of rotations of all nearest neighbors are added up and multiplied by the acceleration α. Specifically, we use

$$\vec{F}^i{}_{\text{CIL}} = \alpha \sum_j s_{ij} \left(\hat{e}_z \times \frac{\vec{v}_i}{|\vec{v}_i|} \right),$$

where

$$s_{ij} = \begin{cases} -\text{sign}\left(\frac{\vec{v}_i}{|\vec{v}_i|} \times \vec{r}_{ij} \right) \cdot \hat{e}_z, & |\vec{r}_{ij}| < 2.5\lambda \text{ and } \vec{v}_i \cdot \vec{r}_{ij} > 0 \\ 0, & \text{otherwise} \end{cases}$$

In simulations where velocity alignment rather than CIL is used (Fig. S4), we replace $\vec{F}_{\text{CIL}}$ by an alignment interaction $\beta \vec{V}_i / |\vec{V}_i|$ with strength β, which is implemented as a constant acceleration in the direction of the average velocity $\vec{V}_i = \langle \vec{v}_j \rangle_{j \in NN_i}$ of nearest neighbors within an interaction range of radius 2.5λ.

Finally, cell division is implemented with a constant probability νdt of dividing, provided there is sufficient space for the appearance of new cells. In a division event, a cell produces a daughter cell in its direct neighborhood with an initial velocity pointing away from the mother cell.

The simulation is performed in nondimensional units such that $\gamma^{-1} = \lambda = 1$. We use the parameters $\sigma^2 = 2$, $\nu = 0.1$, and vary ε between 0.1 and 40, and α between 0 and 12. We initialize $N = 37$ particles within the initial confinement radius R. The stochastic trajectories of the model are then simulated by stepwise Euler updates with a time-step of $dt = 10^{-3}$. We first perform a pre-equilibration run with a confinement potential at $r = R$, modeling the initial confinement phase. At $t = 0$, we remove the boundary by setting the confinement potential to zero, leading to the spreading of the simulated cluster.

Statistical evaluation

For statistical analysis of the data, one-way analysis of variance (ANOVA) followed by Dunnett's multiple comparisons test was performed using GraphPad Prism version 8.0.0 for Windows (GraphPad Software, San Diego, CA, www.graphpad.com); n.s. = not significant, $*p < 0.05$, $**p < 0.01$.

RESULTS AND DISCUSSION

Release from a micropatterned circular adhesive area leads to collective cell spreading

To generate an experimental setup for tracking collective cell-spreading dynamics, we developed a micropatterned platform from which cells can be released in a standardized manner. Specifically, we designed a new patterning approach based on a novel sequence of surface plasma treatment, standard microcontact printing, fibronectin coating, and click-chemistry steps. This process results in the production of 100-μm radius circular fibronectin-coated adhesive areas that are surrounded by cell-repellent azido (PLL-g-PEG) (APP)-coated surfaces. These nonadhesive surfaces can then be activated on demand, via a biocompatible click-chemistry reaction between the azide groups of

the APP on the surface and added BCN-RGD peptides to allow time-controlled cell migration outside the circular areas (56) (see Materials and Methods and Fig. 1). Subsequently, we use T24 urothelial bladder carcinoma epithelial cells which is a well-established malignant cell line (57), widely used in cell migration research (58–61) and in EMT transition (61). The cells are detectable using fluorescence microscopy imaging via their nuclear H2B-GFP fluorescent tag.

We perform time-lapse fluorescence and bright-field microscopy for the first 24 h after surface activation. Here, we observe cells increasingly spreading outward over time, in all directions, covering a large circular area (Fig. 2 *A*, Video S1). To gain access to the dynamics of the entire cell collective, we perform tracking of the fluorescently tagged nuclei (Video S2) as previously described (45), giving access to the full ensemble of cell trajectories (Video S3) in each escaping cluster (Fig. 3 *B*).

As shown by the space-time trajectories of the system, the cells have an overall tendency to spread outward from the initial confinement, and after a period of 10 h, a large fraction of the cells has left the initial confinement (Fig. 3 *A*).

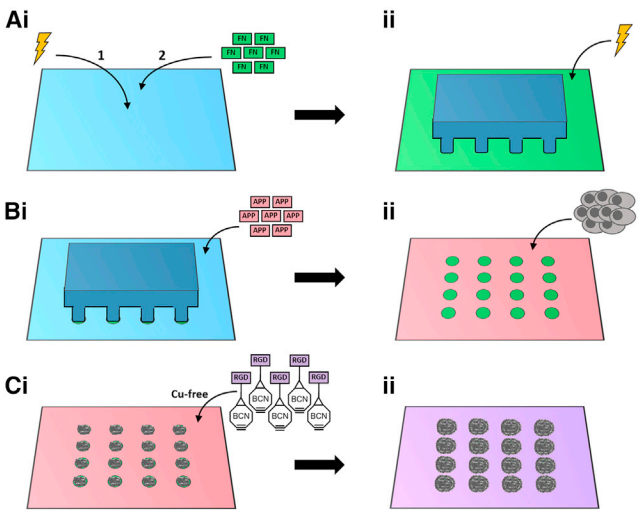

FIGURE 1 Schematic representation of the microcontact printing and click-chemistry process. (*A* i) Ibidi's uncoated surface (here one well is represented) undergoes plasma treatment to become reactive, for subsequent attachment of fibronectin (FN). (*A* ii) Example of PDMS-square stamp with circular patterns produced with standard microcontact printing techniques (*blue*). The stamp is placed at the center of the well and the surface is plasma-treated again. The whole surface except for the stamp-protected circular areas loses its fibronectin coating and becomes hydroxylated. (*B* i) With the stamp remaining in place, APP is added next to it and absorbed by the whole surface except for the stamp-protected circular areas (*green*). (*B* ii) This results in 100-μm radius fibronectin-coated circular areas (*green*) surrounded by an otherwise cell-repellent APP surface (*red*). T24 cancer cells are seeded on the circular areas forming the initial cell population. (*C* i) BCN-RGD peptides are then added and bind to the APP coated surface via click-chemistry reaction between the BCN and the azide groups of the APP. (*C* ii) The previously cell-repellent surface is now coated with RGD and thus, highly cell-adhesive. The cells are able to expand (migrate) from the circular areas to the rest of the surface.

The spreading process is quantified by the evolution of the radial density profile $\rho(r)$ of the cluster (Fig. 3 *B* and *C*). Specifically, we calculate the average number of cells per area element as a function of the distance to the center of the initial confinement radius. As a function of time, the density within the confinement initially decreases, due to cells leaving the confinement through random migration. Correspondingly, the density outside the confinement increases. Interestingly, after a period of approximately 10 h, the density inside the confinement stabilizes at a constant value. To further quantify the overall spreading, we calculate the average radius at which the density profile has decayed to half its value at the center of the initial confinement $R_{1/2}$ (Fig. 3 *D*). The spreading of the cluster appears to be determined both by the movement of cells, as well as cell proliferation (Video S1). To quantify proliferation, we track the number of cells as a function of time (Fig. S2), which reveals that the number of cells doubles within 10 h. Furthermore, we manually track the number of cell divisions in each frame (approximately 5-min difference between frames) in outer ring (edge) versus the inner area (core) of the cluster. We show that divisions are equally distributed across the colony (Fig. S8). This is true not only for the untreated condition (mean diff. $_{\text{core-edge}} = -2.1 \pm 1.7$; $p = 0.27$), but also for the E-cadherin blocking antibody condition (mean diff. $_{\text{core-edge}} = -2.7 \pm 1.7$; $p = 0.18$) as well as the N-cadherin blocking antibody condition (mean diff. $_{\text{core-edge}} = -0.02 \pm 1.4$; $p = 0.99$). Finally, to quantify migration, we measure the average radial velocity of the spreading cells as a function of time, which reveals a marked peak at intermediate spreading times (Fig. 3 *E*).

These statistics are helpful to investigate the impact of collective effects. Thus, we analyzed clusters initialized in the same confinement radius, but with lower cell concentrations. At these lower concentrations, less spreading is achieved (Fig. 3 *D*), and the peak in radial velocity disappears (Fig. 3 *E*), indicating that the dynamics observed in our experiments are density dependent, and therefore have a distinct collective character. Together, these results indicate that release from a micropatterned area leads to the spreading of cell clusters with distinct collective character.

Collective spreading of T24 cancer cells is driven by single-cell migration with transient contacts

Having established the collective character of the spreading process, we next seek to determine whether this expansion is driven by the outward motion of leader cells attached to a confluent monolayer by cell-cell adhesions (62,63), or whether this process is dominated by stochastic single-cell migration with transient cell-cell contacts. To this end, we performed high-resolution cytoskeletal imaging with staining of actin and γ-Tubulin (Figs. 2 *B* and S9). These experiments revealed that, both at early and late time points, the

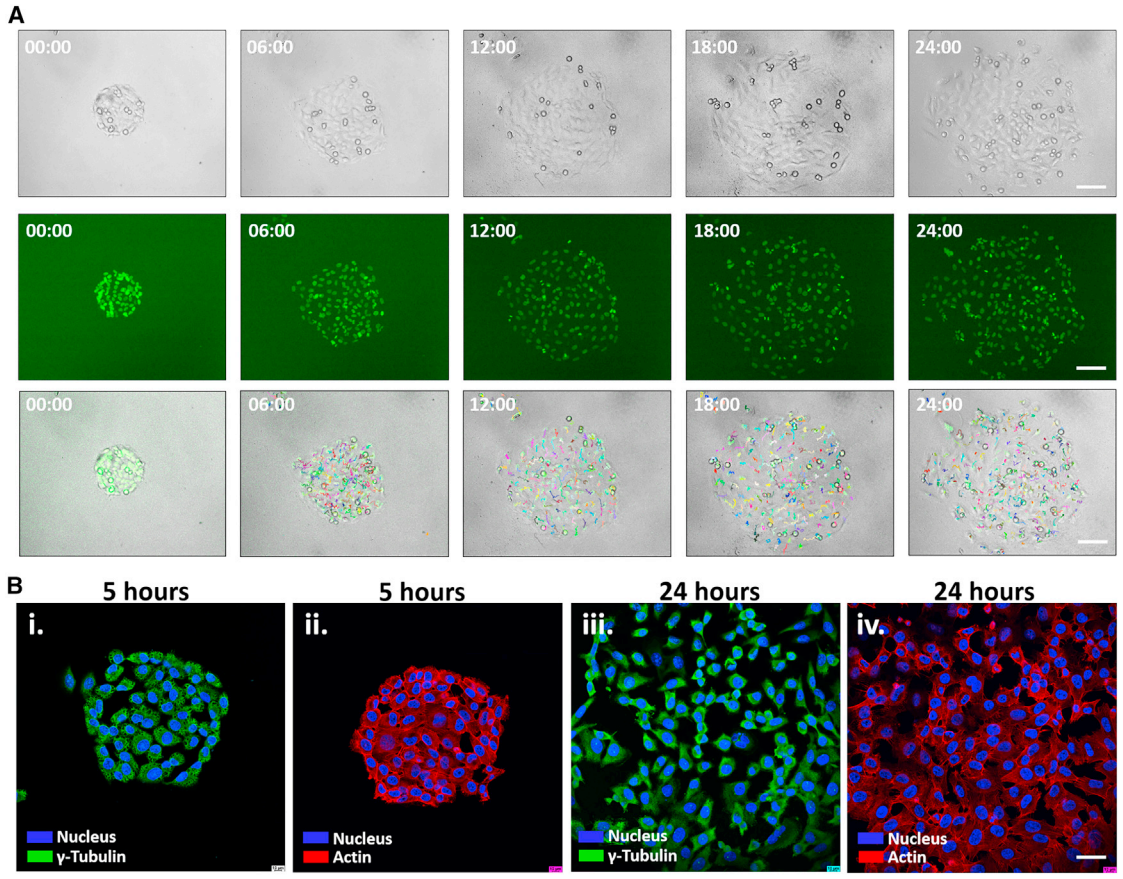

FIGURE 2 Cell spreading time-lapse and cytoskeletal staining of untreated (control) colonies. (*A*) Time-lapse bright-field (upper), fluorescence (middle) microscopy images or overlay with cell tracks (lower) showing the T24 cell migration with 6-h intervals from 0 h to 24 h after surface activation. Scale bar, 100 μm. (*B*) representative confocal images of colonies at 5 h after surface activation with γ-Tubulin + nucleus staining (i) or actin + nucleus staining (ii). The same colonies at 24 h after surface activation are shown in (iii) and (iv), respectively. Scale bar, 50 μm. The cytoskeletal stainings were performed to enable better visual detection of the cell boundaries. Cell clusters are not confluent and a high number of gaps between the cells can be observed.

cell colonies are not fully confluent, as there are significant gaps within the cluster. Furthermore, we found no evidence for the presence of leader cells at the edge of the cluster. Our cytoskeletal staining showed no apparent prevalence of cells with large lamellipodia (a characteristic of leader cells (64,65)) at the edge of the monolayer compared with the rest of the inner reservoir. There were also no apparent actomyosin cables at the colony boundaries or finger-like structures invading the free space that are associated with leader cells (66–68).

We next turned to the time-lapse imaged trajectories to further quantify the nature of collective motion in this system. At the single-cell level, these trajectories are highly stochastic, as expected from single cells that perform persistent random motion on unstructured 2D substrates (12) (Fig. 3 *A*). Furthermore, time-lapse imaging reveals significant stochastic motion of single cells and frequent nearest-neighbor rearrangements during the spreading process (Video S1). To quantify the degree of stochasticity in the collective spreading, we calculate the order of the expansion through the dilatational order parameter *D*, defined to be 1 for perfectly ordered expansion, and 0 for disordered motion (Materials and Methods). This quantity is distinct from the radial velocity, which instead measures the magnitude of the collective motion rather than its order. Interestingly, we observed an average order parameter of 0.1, indicating a large degree of disorder in the spreading process (Fig. 3 *G*). Finally, we investigated the origin of the observed peak in the radial velocity by measuring the radial speed as a function of position within the cell cluster (Fig. 3 *F*). This analysis shows that the onset of radial motion occurs at the periphery of the cluster, and does not spread inward, which is in contrast to previous findings in confluent monolayers of noncancerous cell types (69). Together, these observations suggest that rather than spreading of a confluent, mechanically connected monolayer (62,63), this system exhibits collective motion with predominantly single-cell migration with transient contacts. The collective spreading behavior is therefore likely determined by a combination of single-cell motility, cell proliferation, and transient cell-cell interactions.

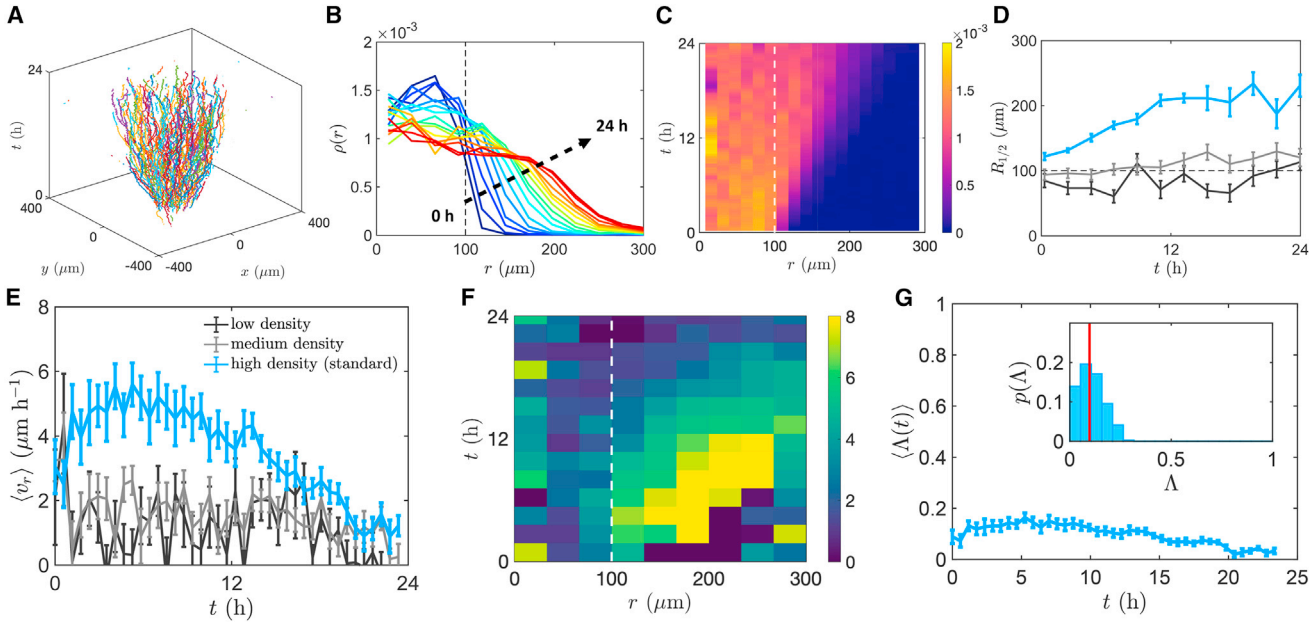

FIGURE 3 Cell spreading and evolution of cell density of control (untreated) T24 cells. (*A*) Space diagram of colony spreading up to 24 h after surface activation. (*B*) Evolution of the density profile over time (*blue* to *red*) plotted as the mean of n = 12 colonies. (*C*) Kymograph of the cell density evolution. Dashed lines indicate the initial confinement radius. (*D*) Average distance where density has decayed to half of its value in the center of the original confinement (i.e., at $r = 0$). (*E*) Mean radial velocity over time for clusters with different initial density. Specifically, the high-density condition corresponds to an average cell number 40 ± 1.5 within the initial confinement. In the medium- and low-density condition, the average cell number within the initial confinement is 18 ± 1.6 and 10 ± 1, respectively. (*F*) Kymograph of the evolution of the radial velocity in space and time (measured in μm/h). *Dashed white line* indicates the initial confinement radius. (*G*) Average dilatational order parameter as a function of time (defined in Materials and Methods). Inset: Probability distribution of observed order parameters; *red line* indicates the average. Error bars: SEM; n = 12 for (*B*), (*C*), (*F*), and (*G*). For (*D*), (*E*): $n_{high} = 12$, $n_{medium} = 15$, $n_{low} = 12$.

Minimal active particle model captures experimental colony spreading

To elucidate the interplay of the various factors affecting the collective migration in our experiments, we developed a minimal active particle model for collective cell migration (Fig. 4 *A*). In this model, single cells perform persistent random motion, as observed for single-cell migration on 2D substrates (10). We included transient cell-cell interactions in our model through two distinct contributions (22,45,55): a repulsive component modeling EV interactions, and CIL, which models the tendency of cells to reorient away from contacts upon collision. Thus, unlike previous models for confluent cell monolayers with elastic (70,71) or attractive (54,72,73) interactions, with this model, we aimed to capture the spreading of a nonconfluent cell layer driven by single-cell migration with transient interactions (Fig. 4 *B*). We first confined the particles into a circular region of radius *R* and then observed their behavior upon release, exactly like in the experiment (Materials and Methods section and Fig. 4 *B*).

Interestingly, this model predicts a rapid decay of the density within the initial confinement area over time, as particles perform random motion and are repelled by their neighbors and move outward (Fig. 4 *C*). This observation is inconsistent with our experimental data, which showed only a weak decay in the initial confinement area (Fig. 3 *D* and *E*). As shown by our cell proliferation estimations, cell division plays an important role on the time-scale of tissue spreading in this system: the number of cells nearly doubles within 10 h (Fig. S2). We therefore included a basic implementation of cell division in our model, where cells stochastically perform divisions at a constant rate. This model including cell division exhibits a slower decay of density, and an overall density profile that is consistent with our experimental observations (Figs. 3 *D* and 4 *D*). This also suggests that divisions play an important role in the experiment by maintaining a high density of the cell layer. This prevents the density from decreasing too quickly, in which case cells would not interact significantly, further supporting the important role of cell proliferation in collective cell-spreading phenomena.

Having included cell division, we found that our model captures other key features of the experimentally observed dynamics. Importantly, we observed that the model predicts a peak in the radial velocity which emerges at the periphery of the colony (Fig. 4 *E* and *F*), similar to experiments (Fig. 3 *E* and *F*). This peak in radial velocity on a time-scale of the order of the persistence time of the cells corresponds to the outward diffusive flux expected for a collection of self-propelled particles (45,74). Specifically, on removal of the

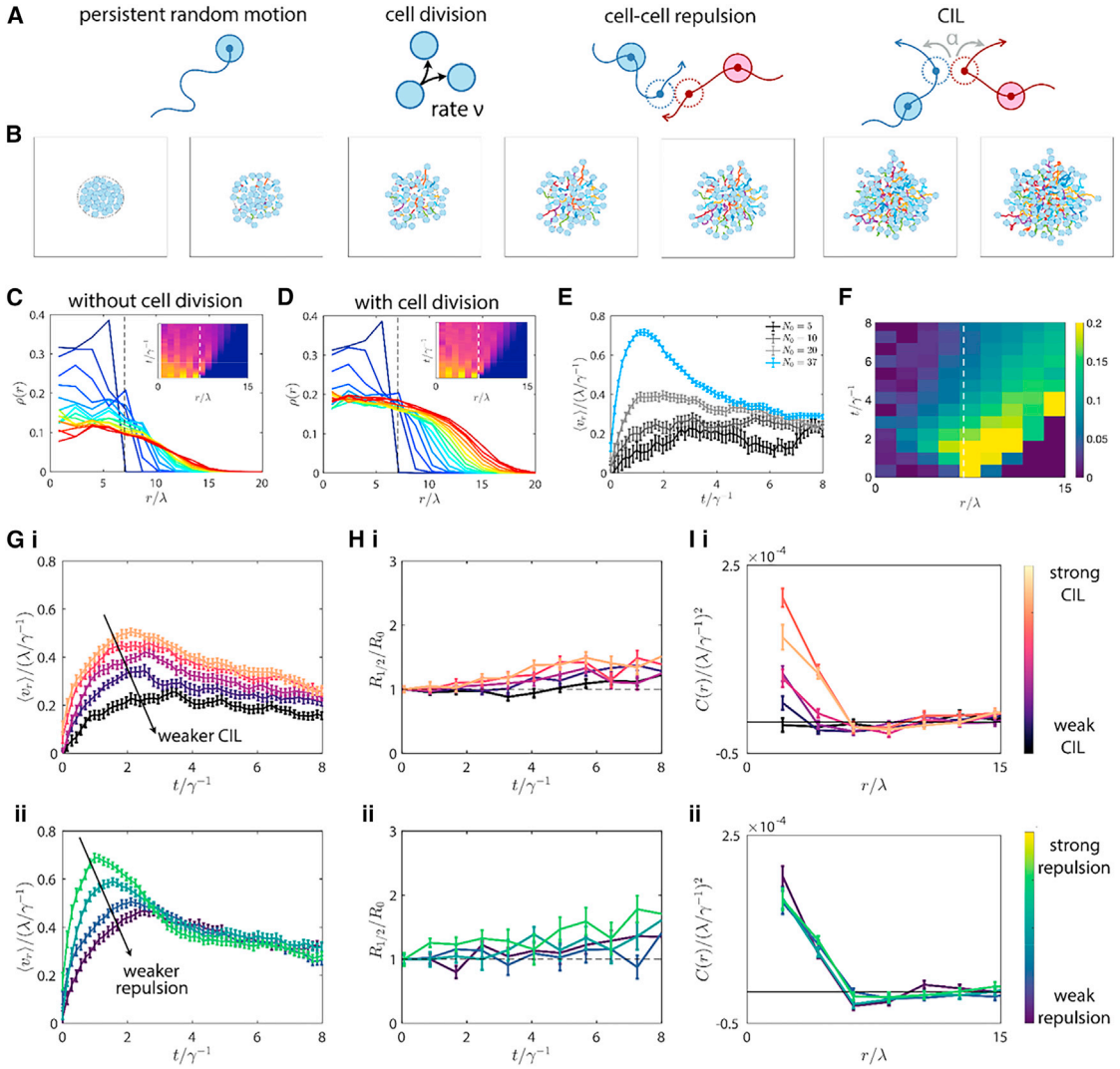

FIGURE 4 Computational model for collective cell spreading. (*A*) Schematic of the components of our active particle model, from left to right: persistent random motion of individual particles, cell division with constant rate ν, EV interactions, and CIL. (*B*) Time-series of a cluster spreading simulation. Cell positions are shown as blue circles of radius λ, which is the radius of the repulsive potential. Previous motion of the cells is shown as colored trajectories. (*C* and *D*) Evolution of the density profile over time (*blue* to *red*) plotted as the mean of n = 30 colonies. Inset: Kymograph of the cell density evolution. *Dashed lines* indicate the initial confinement radius. (*C*) corresponds to a model without cell division, and (*D*) includes cell division. (*E*) Mean radial velocity over time for clusters with different initial density. (*F*) Kymograph of the evolution of the radial velocity in space and time for the model including cell division with high density. *Dashed white line* indicates the initial confinement radius. (*G*) Mean radial velocity over time for (*H*) average distance where density has decayed to half of its value in the center of the original confinement (i.e., at $r = 0$). (*I*) Cross-correlation of velocity fluctuations. Error bars: SEM; n = 30 for all panels. For (*G*, *H*, and *I*): (i) clusters with different CIL interaction amplitudes, (ii) different strengths of cell-cell repulsion interactions.

confinement, cells at the boundary of the cluster are repelled by the bulk of the cluster, leading to a re-orientation of their movement in an outward direction. This causes the initial increase of the average radial velocity, which is followed by a decreasing trend due to the randomization of movement once the cluster has spread significantly (Fig. 4 *G* i). Furthermore, our model reproduces the gradual increase of the spreading radius (Fig. 4 *H* i), and a positive cross-correlation of velocity fluctuations indicating short-ranged alignment of cell movement (Fig. 4 *I* i). Finally, our model correctly predicts a reduction in the radial velocity for lower cell densities, as we observed experimentally (Fig. 3 *E*). Taken together, these results demonstrate that our cell cluster experiments exhibit the behavior expected for a collection of active particles with interactions. In the experiment, the interactions between cells are known to be controlled by transmembrane proteins, including E- and N-cadherins (46,75), whose role we seek to elucidate in the next section.

Effect of blocking antibody treatment on E- and N-cadherin gene and protein expression

To investigate the role of E- and N-cadherin adherens junctions in collective cell migration, we inhibited their function

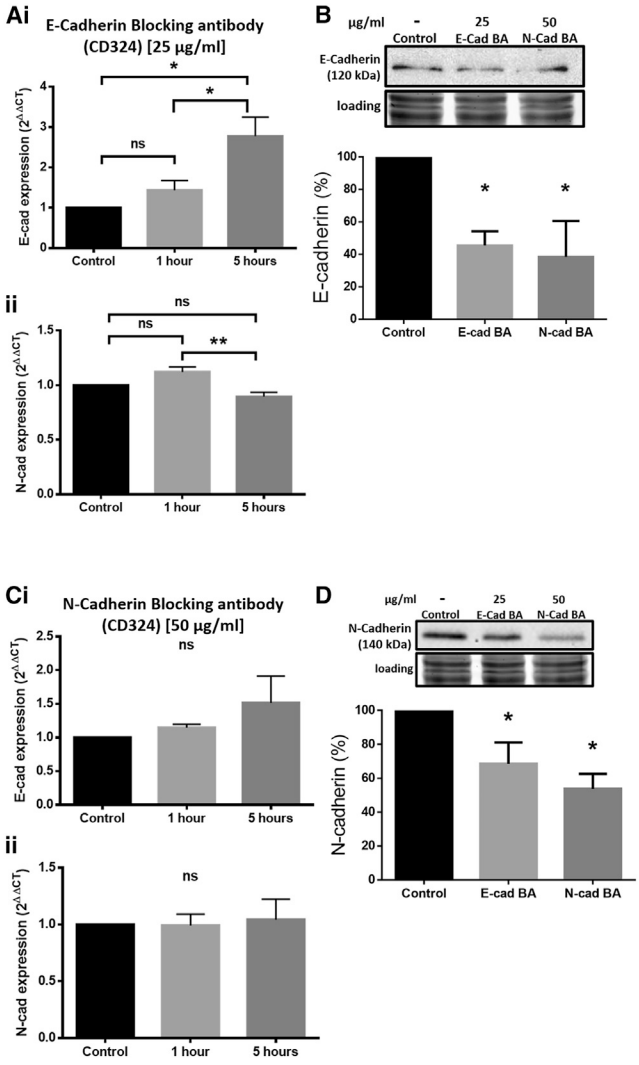

FIGURE 5 Effect of blocking antibody treatment on E- and N-cadherin gene and protein expression. (*A*) Quantitative PCR analysis of (i) E- and (ii) N-cadherin gene expression in untreated (control) or treated T24 cells with E-blocking antibody for 1 and 5 h, respectively. E-cadherin blocking antibody treatment at the highest concentration tested (25 µm/mL) resulted in a significant upregulation of the E-cadherin gene expression after 5 h compared with control (mean diff. ± SE = 1.8 ± 0.43, $p = 0.01$). Furthermore, the same treatment resulted in a significant downregulation of N-cadherin gene expression at the same timepoint compared with the 1-h timepoint, indicating a cadherin-switching effect (mean diff. ± SE = 0.23, ±0.05, $p = 0.009$). (*B*) Quantitative WB analysis of E-cadherin protein levels in untreated (control) or treated T24 cells with 25µg/mL E-cadherin or 50µg/mL N-cadherin blocking antibody after 24 h. Both antibodies significantly reduced the levels of E-cadherin after 24 h (Control versus E-CAD BA: mean diff ± SE = 54.4 ± 19.4, p = 0.03; Control versus N-CAD BA: mean diff ± SE = 61.5 ± 19.4, $p = 0.03$). (*C*) Quantitative PCR analysis of (i) E- and (ii) N-cadherin gene expression in untreated (control) or treated T24 cells with N- blocking antibody for 1 and 5 h, respectively. N-cadherin blocking antibody treatment at the second highest concentration tested (50 µg/mL) resulted in a nonsignificant upregulation of N- and E-cadherin gene expression at 5 h compared with control (N-cadherin: mean diff ±SE = 0.05 ± 0.17, $p = 0.96$; E-cadherin: mean diff ±SE = 0.52 ± 0.33, $p = 0.32$). (*D*) Quantitative WB analysis of N-cadherin protein levels in untreated (control) or treated T24 cells with 25µg/mL E-cadherin or 50µg/mL N-cadherin blocking antibody after 24 h. Both antibodies significantly reduced the levels of N-cadherin after 24 h (Control versus E-CAD BA: mean diff ± SE = 31.4 ± 12.5, p = 0.02; Control versus N-CAD BA: mean diff ± SE = 53.8 ± 12.5, p = 0.02). Untreated cells were used for data normalization. One representative WB is shown per condition including a total protein loading control. Whole WBs are shown in Fig. S3. Statistical analysis was performed using 1-way ANOVA followed by Tukey's multiple comparisons (qPCR) or Sidak's multiple comparisons (WB) test; *$p < 0.05$, **$p < 0.01$; n = 3 (triplicates).

using either E- or N-cadherin blocking antibodies at different concentrations. To assess the effect of E-cadherin blocking antibody on the different cadherin gene expression levels, we performed qPCR for E- and N-cadherin genes at 1 and 5 h after E-cadherin blocking antibody treatment at the highest concentration tested (25 µg/mL). The qPCR served as a short-term indicator of compensatory reactions of the cells upon functional blocking of an adhesion molecule in the crucial 5-h time window after activation. This 5-h timepoint coincides with the peak spreading velocities in the control condition and is therefore of particular interest. We find a significant upregulation of the E-cadherin gene expression after 5 h compared with control (Fig. 5 *A* i). This increase can be considered as a compensatory mechanism of the cell to normalize its E-cadherin functionality after the antibody-mediated blockage. Furthermore, the same treatment results in an early slight upregulation followed by significant downregulation of N-cadherin gene expression at 5 h (Fig. 5 *A* ii). The latter result indicates that the upregulated E-cadherin blocks the expression of N-cadherin (76,77), which may correspond to a known phenomenon called cadherin switching (extensively reviewed by Loh et al. (29)). Moreover, using western blot (WB), we evaluated the effect of E- or N-blocking antibody on E-cadherin protein levels, as WB provides a longer timescale endpoint image of the blocking effect on the total E-cadherin levels. Here, we observed a significant downregulation of E-cadherin at 24 h after treatment with the E-cadherin blocking antibody, verifying the antibody functionality. E-cadherin is also downregulated after N-cadherin blocking antibody treatment (Fig. 5 *B*), which further implies the presence of a cadherin-switching effect. Specifically, the N-cadherin blocking antibody could transiently increase the gene expression of N-cadherin, as a compensatory mechanism, which in turn could represses E-cadherin expression. Interestingly, for E-cadherin in the control (untreated) condition, we detected multiple shorter bands rather than one band of 130 to 135 kDa, which is the normal size of the protein. The observed bands were a size of approximately 120 kDa, 95 kDa, and 55 kDa (as shown in Fig. S3, respectively). Such deviations from the 135-kDa range, involving predominantly a soluble 80-kDa species (78–80), as well as 97-kDa (81), 48-kDa (82), and 23-kDa (83) fragments are common in the literature and have been associated with the development of different cancer types (29) (84,85). Therefore, as E-cadherin protein expression is known to be very limited (41) or nonexistent (42,43)

in T24 cells, it is probable that the shorter E-cadherin fragments we see are a result of protein degradation.

We then investigated the effect of N-cadherin blocking antibody on cadherin gene expression levels, by performing qPCR for E- and N-cadherin genes 1 h and 5 h after N-cadherin blocking antibody treatment at the second highest concentration tested (50 μg/mL). In that case, a slight tendency toward upregulation of E-cadherin gene expression is observed at 5 h compared with control (Fig 5 *C* i), whereas the N-cadherin expression levels were not significantly different from untreated cells (Fig. 5 *C* ii). This lack of significance could result from the fact that in T24 cells, the presence of N-cadherin is much higher compared with E-cadherin (41), and thus a higher concentration of blocking antibody would be required for a stronger effect. However, we observed the clear long-term influence of E- or N-blocking antibody on N-cadherin protein levels by WB where we identify a significant downregulation of N-cadherin protein levels at 24h after E- and N-cadherin blocking antibody treatment (Fig. 5 *D*). Therefore, we conclude that treatment with either E- or N-cadherin blocking antibody starts with a transient upregulation in the corresponding cadherin gene expression, which in turn leads to activation of the cadherin-switching mechanism that results in the downregulation of the opposite cadherin. This result is further verified by the WB results, where E- or N-cadherin protein levels are significantly downregulated when cells are treated with opposite blocking antibody over the long-term 24-h timepoint. With regard to the WB-detected N-cadherin bands in the untreated condition, a clear band at the expected size (140 kDa) is always observed, suggesting that there was no apparent degradation or soluble form, as was the case for E-cadherin. This is not surprising, as N-cadherin is the predominant and fully functional cadherin in the T24 cell line (41,86). In summary, these findings verify that 1) there is a low gene and protein expression of functional (membrane-bound) E-cadherin in our T24 cells (Fig. S3 *C* and *D*), and that 2) besides the direct blocking effect, there is an "off-target" blocking effect, where the continuous overexpression of the cadherin being directly blocked leads to a downregulation of the opposite cadherin due to cadherin switching.

To visualize the effect of blocking antibody treatment on E- and N-cadherin junctions, we performed immunofluorescence stainings of colonies at the 5- and 24-h timepoints (Fig. 6). Upon E-cadherin blocking, we observed an evident reduction in the fluorescence intensity of E-cadherin staining at 24 h. This shows that the E-cadherin blocking antibody reduced the amount of functional E-cadherin in the cells 24 h posttreatment, in agreement with our WB results. The fluorescence intensity of N-cadherin staining was not visibly reduced by addition of N-cadherin blocking antibody. Although in the WB experiments we see a clear reduction in the levels of N-cadherin as a result of N-cadherin blocking antibody treatment, the N-cadherin staining was probably not sensitive enough to reflect this effect as a decrease in fluorescence intensity. This suggests that, as T24 cells express much higher of N-cadherin compared with E-cadherin (41), a higher concentration of N-cadherin blocking antibody may be required to induce a visible reduction in the fluorescence intensity. Interestingly, both blocking antibodies resulted in larger gaps between the cells, and slightly elongated cell phenotypes.

Disrupting E- and N-cadherin junctions decreases speed of collective spreading

Having quantified the E- and N-cadherin expression upon different levels of E- or N-cadherin blocking, we moved on to analyzing the collective migration behavior in these conditions. First, we found that a low concentration of E-cadherin blocking antibody (10 μg/mL) does not significantly affect migration behavior such as the colony spreading represented by density profiles and radial velocities of the cells (Fig. 7 *A*, *B* i, *C* i, *D* i, *D* ii; Video S4). However, blocking E-cadherin at a higher concentration of antibody (25 μg/mL) reduces the average spreading of the colonies (Fig. 7 *B* ii, *C* ii, and *D* ii), as well as the average radial velocity of the cells (Fig. 7 *D* i). Similarly, increasing concentrations of N-cadherin blocking antibody leads to reduced average colony spreading and radial velocities, with the highest one (100 μg/mL) having the strongest effect (Fig. 8 *A*, *B*, *C*, *D* i, *D* ii; Video S5). In contrast, we found that the average velocity of single migrating cells in experiments with sparsely seeded cells is not significantly affected by the addition of either blocking antibody, for the whole duration of the experiment (Fig. S1). Furthermore, the proliferation of cells is similar across all conditions (Fig. S2). These observations suggest that the change in spreading behavior upon cadherin blocking is not mediated by changes in the behavior of single cells or their proliferation, but is mainly caused by the reduction in cell-cell interactions and is thereby a collective effect.

To identify a possible change in cell-cell interactions due to cadherin blocking, we calculated the cross-correlation functions of velocity fluctuations between pairs of cells, which quantifies how similar cellular velocities are as a function of their distance from one another (Materials and Methods section; Figs. 7 *D* iii and 8 *D* iii). As expected, in the control condition, we found that cells tend to align their direction of motion with neighboring cells, but exhibit no correlations at long distances. Unexpectedly, however, we found that all observed experimental conditions have a similar cross-correlation function. This indicates that although we expect a change in cell-cell interactions to be responsible for the change in spreading behavior, this change does not directly affect the degree of velocity alignment, quantified through the velocity cross-correlation. In a following section, we turn to a theoretical model for a possible explanation of these observations.

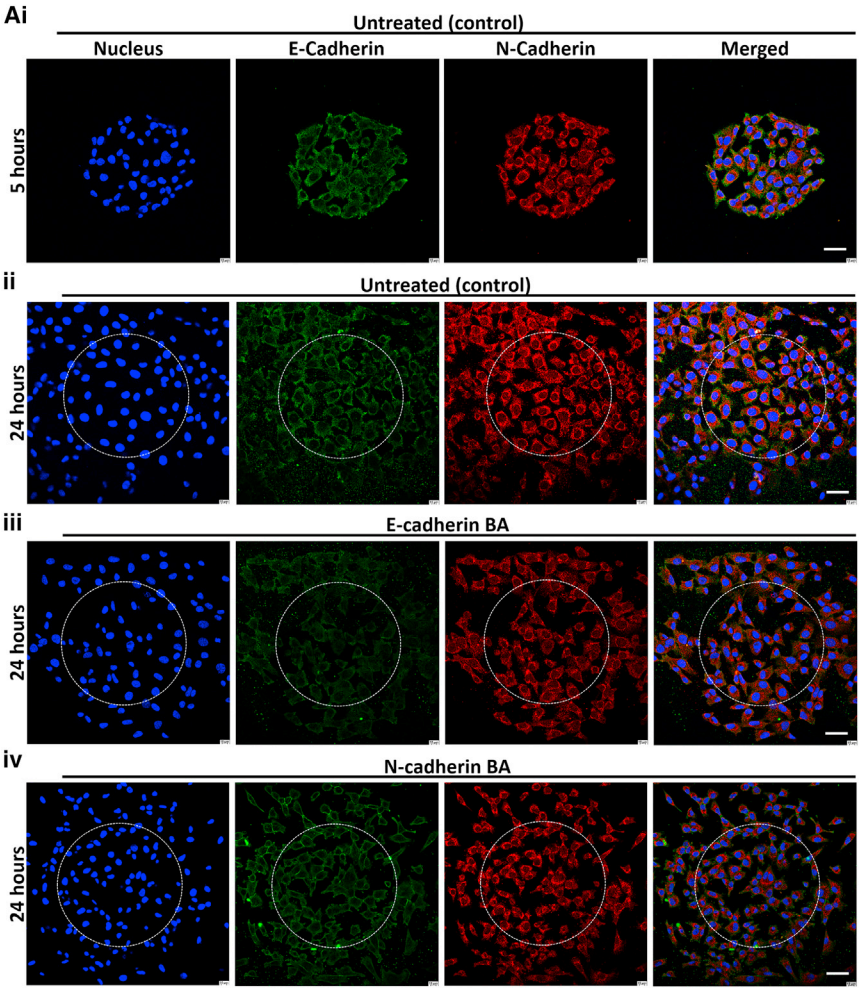

FIGURE 6 E- and N-cadherin immunofluorescence staining of untreated (control) and E- or N-cadherin BA-treated colonies. Representative confocal images of untreated (control) colonies costained against E- and N-cadherin (*green* and *red*, respectively), together with nuclear labeling (*blue*), at 5 h (i) and 24h (ii) after surface activation. (iii) Cadherin-stained colonies upon E-cadherin blocking antibody treatment (25 μg/mL) at 24 h after surface activation, (iv) cadherin-stained colonies upon N-cadherin blocking antibody treatment (100 μg/mL) at 24 h after surface activation. *Dashed circles* show the original confinement of the clusters. Merge is shown on the right column. Scale bar: 50 μm.

To summarize our experimental findings, we found that by partially blocking either E- or N-cadherin adherens junctions, the collective spreading behavior of initially confined clusters of T24 cells becomes less efficient. This suggests that cell-cell contacts are important for coordinated migration, possibly by promoting cell-cell interactions. This result is in agreement with earlier reports showing that preventing cells from forming stable cell-cell contacts resulted in uncoordinated and random cell movement (87), leading to significantly lower migration velocities (88). In contrast to other studies observing no E-cadherin expression in T24 cells, we detected its presence (120 kDa) among other fragmented species of the protein. Furthermore, we showed that as a type III carcinogenic line, T24 cells exhibit an increased N-cadherin versus E-cadherin expression ratio (3/1 as shown in Fig. S3 *C* and *D*), characteristic for EMT (29). Interestingly, we found that the limited E-cadherin expression is still important for the efficiency of the collective migration, as is the more predominantly expressed N-cadherin. Therefore, the interplay between E- and N-cadherin in T24 cells points to a crucial balance in cell-cell contacts that seems to be important for collective migration. In the next section, we use our minimal active particle model to elucidate the nature of these interactions and how they influence the cell-spreading behavior.

Varying cell-cell interactions in a minimal active particle model captures the effects of cadherin blocking

To investigate how changes in cell-cell interactions affect the spreading behavior in our model, we first varied the strength of CIL. We implemented CIL as an angular repulsion that acts as a torque on cells undergoing a contact, with strength α, similar to previous work (45) (see Fig. 4 *A*; Materials and Methods section). We find that decreasing α, corresponding to weaker CIL, leads to a reduction in radial velocity, spreading, and cross-correlations (Fig. 4 *G* i, *H* i, and *I* i). Thus, although the first two findings are in line with the changes in behavior upon cadherin inhibition in the experiment, the change in cross-correlation is not observed in the experiment. In contrast, reducing the strength of the repulsive interactions between particles leads to a reduction of the radial velocity peak and the overall

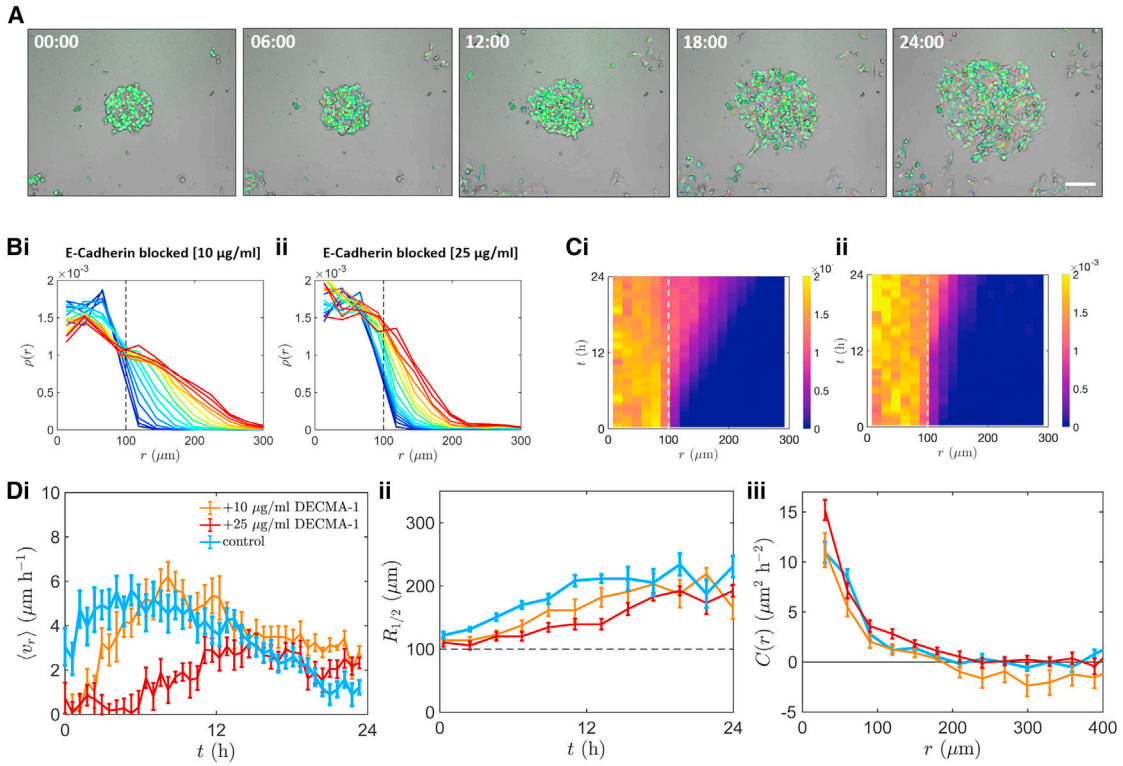

FIGURE 7 Evolution of cell density profile, radial velocities, and average distance of T24 cells treated with increasing concentrations of E-cadherin blocking antibody. (*A*) Time-lapse overlay of bright-field and fluorescence microscopy images with cell tracks of the 25 μg/mL E-cadherin blocking, showing the T24 cell migration with 6-h intervals from 0 h to 24 h after surface activation. (*B*) Evolution of the density profiles over 24 h (*blue* to *red*) plotted as the mean of all colonies per condition for T24 cells treated with (i) 10 μg/mL or (ii) 25 μg/mL E-cadherin blocking antibody. All curves are separated by 1-h intervals. (*C*) Kymographs of the cell density evolution, for T24 cells treated with (i) 10μg/mL and (ii) 25 μg/mL E-cadherin blocking antibody. (*D* i) Mean radial velocity (u_r) over time (average of all colonies per condition). The control condition exhibited a direct increase in radial velocity, peaking around 5 h after surface activation (*blue*); 10 μg/mL E-cadherin blocking antibody slowed down this increase in radial speed, which peaked at 8 h (*orange*). The highest concentration of blocking antibody (25 μg/mL) resulted in even lower radial velocity that did not reach the initial peaks exhibited in the other conditions (*red*). (ii) Average distance where density has decayed to half of its value in the center of the original confinement (i.e., at $r = 0$). The distance was the highest over time in the control condition and decreased with increasing concentrations of E-cadherin blocking antibody. (iii) Cross-correlation of velocity fluctuations showing no significant differences between conditions. Error bars, SEM; $n_{control} = 12$, $n_{10ECAD} = 13$, $n_{25ECAD} = 8$.

spreading, while keeping the cross-correlations constant (Fig. 4 *G* ii, *H* ii, and *I* ii), similar to what we observed experimentally upon blocking E- or N-cadherin-mediated intercellular contacts (Fig. 7 *B* ii, *D*, 8 *B* ii, iii, and *D*). These results are robust over a wide range of parameters in the model (Figs. S5 and S6). These observations suggest that disrupting cell-cell junctions through E and N-cadherin blocking has an effect akin to reducing EV interactions between cells.

The reduced spreading for weaker CIL and weaker repulsive interactions can be understood intuitively. First, CIL interactions ensure that cells at the cluster boundary do not cross paths, leading to outward alignment of their velocities. In fact, in this setup, CIL has an effect very similar to velocity alignment interactions: an alternative model with velocity alignment instead of CIL produces very similar results (Fig. S4), highlighting the similarity of these two interaction types in this setup. Second, repulsion ensures that boundary cells are repelled by the bulk of the cluster, which further rectifies their motion into a radially outward direction. Thus, both stronger CIL and stronger repulsive interactions lead to faster, more efficient spreading dynamics (Fig. 4 *G* and *H*).

However, we can distinguish the two types of interaction through the cross-correlation of cell velocities: this quantity serves as a good indicator for changes in CIL behavior. Specifically, changing repulsive interactions has no significant effect on the correlation function, because it is a position-dependent interaction (Fig. 4 *I* ii). In contrast, CIL is a velocity-dependent interaction, and its strength therefore controls the magnitude of the velocity cross-correlations (Fig. 4 *I* i). Therefore, our results suggest that rather than reducing the strength of CIL behavior, disrupting cell-cell junctions through E- and N-cadherin blocking has an effect akin to reducing repulsive interactions between cells.

To further test this finding experimentally, we assessed cell polarization using cytoskeletal staining, as previously described (49). First, we showed that the number of cells polarized toward cell-cell contacts is not significantly different from the number of cells polarized away from

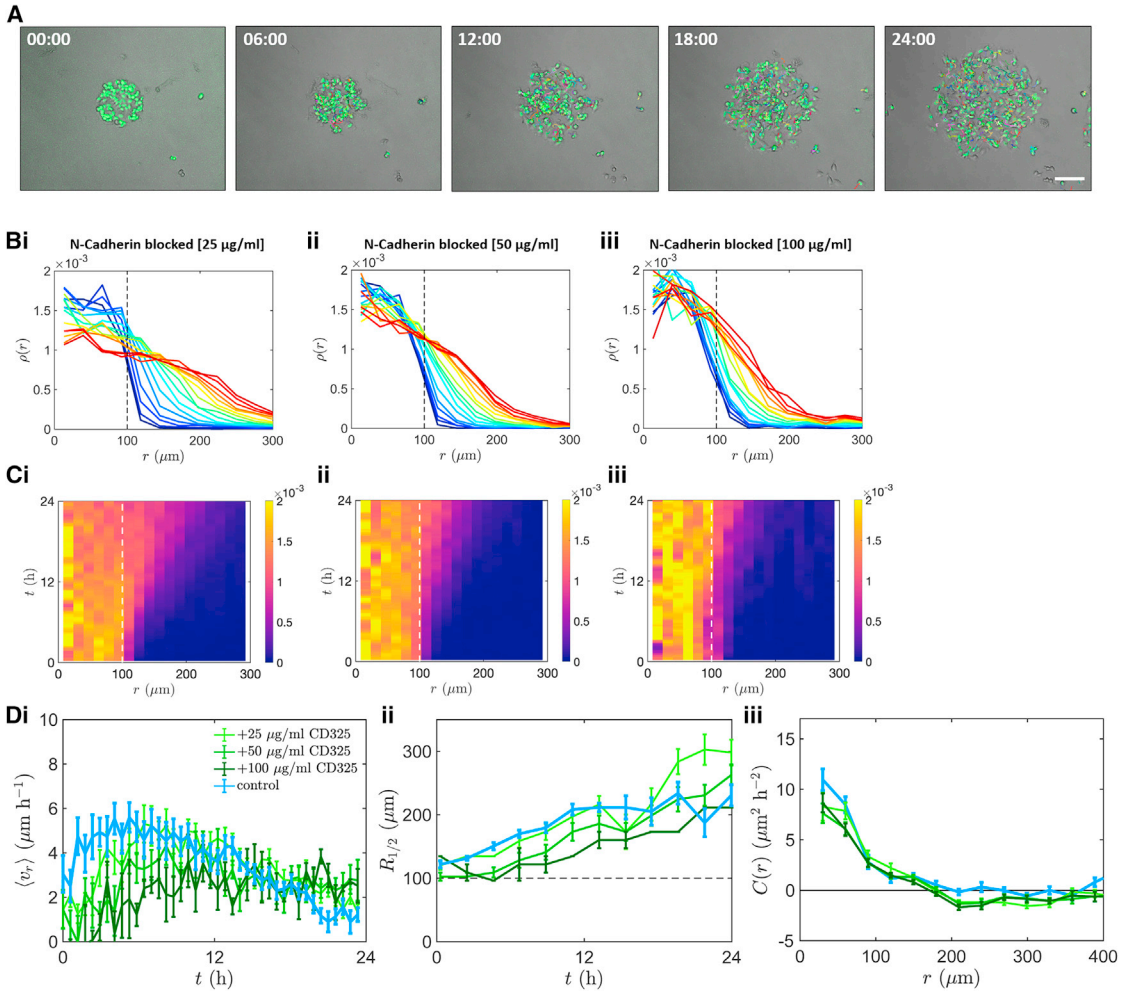

FIGURE 8 Evolution of cell density profile, radial velocities, and average distance of T24 cells treated with increasing concentrations of N-cadherin blocking antibody. (*A*) Time-lapse overlay of bright-field and fluorescence microscopy images with cell tracks of the 100 μg/mL N-cadherin blocking, showing the T24 cell migration with 6-h intervals from 0 h to 24 h after surface activation. (*B*) Evolution of the density profiles over 24 h (*blue* to *red*) plotted as the mean of all colonies per condition for T24 cells treated with (i) 25 μg/mL, (ii) 50 μg/mL, or (iii) 100 μg/mL N-cadherin blocking antibody. All curves are separated by 1-h intervals. (*C*) Kymographs of the cell density evolution, for T24 cells treated with (i) 25 μg/mL, (ii) 50 μg/mL, or (iii) 100 μg/mL N-cadherin blocking antibody. (*D* i) Mean radial velocity (u_r) over time (average of all colonies per condition). The control condition exhibited a direct increase in radial velocity, peaking around 5 h after surface activation (*blue*). Increasing concentrations of N-cadherin blocking antibody reduced this increase in radial speed, with the highest reduction observed in the 100μg/mL treated cells (*dark green*). (ii) Average distance where density has decayed to half of its value in the center of the original confinement (i.e., at $r = 0$). The distance was the highest in the control condition and decreased with increasing concentrations of N-cadherin blocking antibody up to 11 h. After this timepoint, the 25 μg/mL N-cadherin blocking antibody-treated colonies surpassed the control ones. (iii) Cross-correlation of velocity fluctuations showing no significant differences between conditions. Error bars, SEM; $n_{control} = 12$, $n_{25NCAD} = 8$, $n_{50NCAD} = 6$, $n_{100NCAD} = 3$.

cell-cell contacts (mean diff $_{away\text{-}toward} = 13 \pm 6.5$, $p = 0.07$; Fig. S7). Furthermore, we performed the same quantification for the E- and N-cadherin blocking conditions and found that blocking of either cadherin type did not induce significant changes in this type of cell polarization behavior compared with the control condition (1-way ANOVA for the ratio [perc. cells polarized away/perc. cells polarized toward]: $F = 2.4$; $p = 0.14$; Fig. S7).

Taken together, our experimental and modeling results show that cell-cell interactions are key drivers of tissue spreading in this setup, and that disrupting cell-cell junctions through E- and N-cadherin blocking has an effect akin to reducing repulsive interactions between cells. Specifically, the congruity between experiment and model suggests that both E- and N-cadherin-mediated intercellular contacts create repulsive events via EV interactions that are critical for the efficient cell spreading during collective migration. This effect could be due to cadherins "sharpening" cell boundaries by, e.g., regulating cell shape, improving cell-cell recognition, or increasing interfacial tension. Indeed, both E- and N-cadherin have been shown to determine intercellular interfacial tension in the developing epithelium (46,89,90). Our results challenge the prevalent view in the literature that E- and N-cadherin junctions are essential for CIL (91–96); however, our findings are not entirely unexpected, as there are other studies showing an

opposing role between the different cadherin types in CIL, with E-cadherin inhibiting CIL and N-cadherin promoting CIL, in cells undergoing EMT to become migratory (97,98). Therefore, the role of cadherins in CIL during collective spreading may differ between cell lines (noncancerous versus cancerous, epithelial versus mesenchymal). These results are also in qualitative agreement with previous work where the interactions of colliding pairs of cells were inferred directly from observed trajectories (55). Specifically, it was shown that the cancerous MDA-MB-231 cell line exhibits less repulsive interactions than the nonmalignant MCF10A cell line, which is known to exhibit higher E-cadherin expression than MDA-MB-231 cells (99,100). Our work, therefore, further supports the important role of cadherin-mediated cell-cell interactions, and elucidates their role in collective cell migration.

CONCLUSION

This study provides new insight into the role of different cadherin junctions in the dynamics of collective cancer cell migration. In our setup, we find that the collective migration of T24 cancer cells is predominantly driven by stochastic single-cell migration with transient cell-cell contacts. We reveal that in this case, blocking E- or N-cadherin in collectively migrating T24 cancer cells significantly reduces their spreading efficiency. The observed phenomenology is well captured by a biophysical model of stochastically migrating cells. Our model shows that cell proliferation as well as the EV and CIL interactions between cells drive tissue spreading in our setup. Our combined experimental and theoretical results further indicate that disrupting E- and N-cadherin-mediated intercellular contacts leads to a decrease in repulsive cell-cell interactions, which in turn reduces the spreading efficiency of the cell collective. Therefore, from a biomedical point of view, this study underscores the importance of E- and N-cadherins as potential pharmacological targets in metastatic cancer research. Furthermore, our experimental setup design could be adapted for future research in the field, such as studying the impact of mechanical cell-cell communication on cell spreading on mechanically compliant substrates (101–103), or chemotactic cell spreading in external gradients (104,105).

SUPPORTING MATERIAL

Supporting material can be found online at https://doi.org/10.1016/j.bpj.2021.12.006.

AUTHOR CONTRIBUTIONS

T.Z., D.B.B., C.P.B., and S.Z. designed the study. T.Z. performed all experiments. J.A. contributed tracking software. D.B.B. and T.Z. analyzed data. D.B.B. and T.B. developed the theoretical model. T.Z. and D.B.B. wrote the paper with input from all authors.

ACKNOWLEDGMENTS

Funded by the Deutsche Forschungsgemeinschaft - Project-ID 201269156 - SFB 1032 (Projects B8 and B12). D.B.B. is a NOMIS Fellow supported by the NOMIS Foundation and was supported in part by a DFG fellowship within the Graduate School of Quantitative Biosciences Munich (QBM) and by the Joachim Herz Stiftung.

REFERENCES

1. Friedl, P., and D. Gilmour. 2009. Collective cell migration in morphogenesis, regeneration and cancer. *Nat. Rev. Mol. Cell Biol.* 10:445–457.
2. Rey-Barroso, J., D. S. Calovi, …, L. Dupré. 2018. Switching between individual and collective motility in B lymphocytes is controlled by cell-matrix adhesion and inter-cellular interactions. *Sci. Rep.* 8:5800.
3. Grada, A., M. Otero-Vinas, …, V. Falanga. 2017. Research techniques made simple: analysis of collective cell migration using the wound healing assay. *J. Invest. Dermatol.* 137:e11–e16.
4. Wood, J. M., and M. F. Olson. 2012. Collective migration: spatial tension relief. *Curr. Biol.* 22:R125–R127.
5. Trepat, X., Z. Chen, and K. Jacobson. 2012. Cell migration. *Compr. Physiol.* 2:2369–2392.
6. De Pascalis, C., and S. Etienne-Manneville. 2017. Single and collective cell migration: the mechanics of adhesions. *Mol. Biol. Cell.* 28:1833–1846.
7. George, M., F. Bullo, and O. Campàs. 2017. Connecting individual to collective cell migration. *Sci. Rep.* 7:9720.
8. Ladoux, B., and R. M. Mège. 2017. Mechanobiology of collective cell behaviours. *Nat. Rev. Mol. Cell Biol.* 18:743–757.
9. Etienne-Manneville, S. 2012. Adherens junctions during cell migration. *Subcell. Biochem.* 60:225–249.
10. Gail, M. H., and C. W. Boone. 1970. The locomotion of mouse fibroblasts in tissue culture. *Biophys. J.* 10:980–993.
11. Metzner, C., C. Mark, …, B. Fabry. 2015. Superstatistical analysis and modelling of heterogeneous random walks. *Nat. Commun.* 6:7516.
12. Selmeczi, D., S. Mosler, …, H. Flyvbjerg. 2005. Cell motility as persistent random motion: theories from experiments. *Biophys. J.* 89:912–931.
13. Brückner, D. B., A. Fink, …, C. P. Broedersz. 2019. Stochastic nonlinear dynamics of confined cell migration in two-state systems. *Nat. Phys.* 15:595–601.
14. Fink, A., D. B. Brückner, …, J. O. Rädler. 2020. Area and geometry dependence of cell migration in asymmetric two-state micropatterns. *Biophys. J.* 118:552–564.
15. Brückner, D. B., A. Fink, …, C. P. Broedersz. 2020. Disentangling the behavioural variability of confined cell migration. *J. R. Soc. Interface.* 17:20190689.
16. Mitterwallner, B. G., C. Schreiber, …, R. R. Netz. 2020. Non-Markovian data-driven modeling of single-cell motility. *Phys. Rev. E.* 101:032408.
17. Dyson, L., and R. E. Baker. 2015. The importance of volume exclusion in modelling cellular migration. *J. Math. Biol.* 71:691–711.
18. Abercrombie, M., and J. E. M. Heaysman. 1954. Observations on the social behaviour of cells in tissue culture: II. "Monolayering" of fibroblasts. *Exp. Cell Res.* 6:293–306.
19. Carmona-Fontaine, C., H. K. Matthews, …, R. Mayor. 2008. Contact inhibition of locomotion in vivo controls neural crest directional migration. *Nature.* 456:957–961.
20. Camley, B. A., and W.-J. Rappel. 2017. Physical models of collective cell motility: from cell to tissue. *J. Phys. D Appl. Phys.* 50:113002.
21. Giniūnaitė, R., R. E. Baker, …, P. K. Maini. 2020. Modelling collective cell migration: neural crest as a model paradigm. *J. Math. Biol.* 80:481–504.

22. Alert, R., and X. Trepat. 2020. Physical models of collective cell migration. *Annu. Rev. Condens. Matter Phys.* 11:77–101.
23. Brückner, D. B. 2020. Learning the dynamics of cell-cell interactions in confined cell migration. *Arxiv*:2008.03978.
24. Schnyder, S. K., J. J. Molina, and R. Yamamoto. 2020. Control of cell colony growth by contact inhibition. *Sci. Rep.* 10:6713.
25. Paulson, A., M. Prasad, …, P. Manzerra. 2014. Regulation of cadherin expression in nervous system development. *Cell Adh. Migr.* 8:19–28.
26. Halbleib, J. M., and W. J. Nelson. 2006. Cadherins in development: cell adhesion, sorting, and tissue morphogenesis. *Genes Dev.* 20:3199–3214.
27. Shapiro, L., and W. I. Weis. 2009. Structure and biochemistry of cadherins and catenins. *Cold Spring Harb. Perspect. Biol.* 1:a003053.
28. Campbell, K., and J. Casanova. 2016. A common framework for EMT and collective cell migration. *Development.* 143:4291.
29. Loh, C.-Y., J. Y. Chai, …, C. Y. Looi. 2019. The E-cadherin and N-cadherin switch in epithelial-to-mesenchymal transition: signaling, therapeutic implications, and challenges. *Cells.* 8:1118.
30. Yu, W., L. Yang, …, Y. Zhang. 2019. Cadherin signaling in cancer: its functions and role as a therapeutic target. *Front. Oncol.* 9:989.
31. Wheelock, M. J., Y. Shintani, …, K. R. Johnson. 2008. Cadherin switching. *J. Cell Sci.* 121:727.
32. Pérez-González, C., R. Alert, …, X. Trepat. 2019. Active wetting of epithelial tissues. *Nat. Phys.* 15:79–88.
33. Ilina, O., P. G. Gritsenko, …, P. Friedl. 2020. Cell–cell adhesion and 3D matrix confinement determine jamming transitions in breast cancer invasion. *Nat. Cell Biol.* 22:1103–1115.
34. Padmanaban, V., I. Krol, …, A. J. Ewald. 2019. E-cadherin is required for metastasis in multiple models of breast cancer. *Nature.* 573:439–444.
35. Bindels, E. M. J., M. Vermey, …, T. H. Van Der Kwast. 2000. E-cadherin promotes intraepithelial expansion of bladder carcinoma cells in an in vitro model of carcinoma in situ. *Cancer Res.* 60:177.
36. Putzke, A. P., A. P. Ventura, …, B. S. Knudsen. 2011. Metastatic progression of prostate cancer and e-cadherin regulation by zeb1 and SRC family kinases. *Am. J. Pathol.* 179:400–410.
37. Reddy, P., L. Liu, …, K. Liu. 2005. Formation of E-cadherin-mediated cell-cell adhesion activates AKT and mitogen activated protein kinase via phosphatidylinositol 3 kinase and ligand-independent activation of epidermal growth factor receptor in ovarian cancer cells. *Mol. Endocrinol.* 19:2564–2578.
38. Lewis-Tuffin, L. J., F. Rodriguez, …, P. Z. Anastasiadis. 2010. Misregulated E-cadherin expression associated with an aggressive brain tumor phenotype. *PLoS One.* 5:e13665.
39. Su, Y., J. Li, …, G. L. Radice. 2016. N-cadherin functions as a growth suppressor in a model of K-ras-induced PanIN. *Oncogene.* 35:3335–3341.
40. Lammens, T., K. Swerts, …, G. Laureys. 2012. N-cadherin in neuroblastoma disease: expression and clinical significance. *PLoS One.* 7:e31206.
41. Elie-Caille, C., I. Lascombe, …, S. Fauconnet. 2020. Molecular and nanoscale evaluation of N-cadherin expression in invasive bladder cancer cells under control conditions or GW501516 exposure. *Mol. Cell. Biochem.* 471:113–127.
42. Lascombe, I., A. Clairotte, …, H. Bittard. 2006. N-cadherin as a novel prognostic marker of progression in superficial urothelial tumors. *Clin. Cancer Res.* 12:2780.
43. Rebel, J. M., C. D. Thijssen, …, T. H. Van der Kwast. 1994. E-cadherin expression determines the mode of replacement of normal urothelium by human bladder carcinoma cells. *Cancer Res.* 54:5488–5492.
44. van Dongen, S. F. M., P. Maiuri, …, M. Piel. 2013. Triggering cell adhesion, migration or shape change with a dynamic surface coating. *Adv. Mater.* 25:1687–1691.
45. d'Alessandro, J., A. P. Solon, …, C. Rivière. 2017. Contact enhancement of locomotion in spreading cell colonies. *Nat. Phys.* 13:999–1005.
46. Maître, J. L., and C. P. Heisenberg. 2013. Three functions of cadherins in cell adhesion. *Curr. Biol.* 23:R626–R633.
47. Fleige, S., V. Walf, …, M. W. Pfaffl. 2006. Comparison of relative mRNA quantification models and the impact of RNA integrity in quantitative real-time RT-PCR. *Biotechnol. Lett.* 28:1601–1613.
48. Chopra, A., W. G. Willmore, and K. K. Biggar. 2019. Protein quantification and visualization via ultraviolet-dependent labeling with 2,2,2-trichloroethanol. *Sci. Rep.* 9:13923.
49. Silverman-Gavrila, R., L. Silverman-Gavrila, …, M. P. Bendeck. 2011. Rear polarization of the microtubule-organizing center in neointimal smooth muscle cells depends on PKCα, ARPC5, and RHAMM. *Am. J. Pathol.* 178:895–910.
50. Kaverina, I., and A. Straube. 2011. Regulation of cell migration by dynamic microtubules. *Semin. Cell Dev. Biol.* 22:968–974.
51. Attanasi, A., A. Cavagna, …, M. Viale. 2014. Collective behaviour without collective order in wild swarms of midges. *PLoS Comput. Biol.* 10:e1003697.
52. Basan, M., J. Elgeti, …, H. Levine. 2013. Alignment of cellular motility forces with tissue flow as a mechanism for efficient wound healing. *Proc. Natl. Acad. Sci. U S A.* 110:2452.
53. Garcia, S., E. Hannezo, …, N. S. Gov. 2015. Physics of active jamming during collective cellular motion in a monolayer. *Proc. Natl. Acad. Sci. U S A.* 112:15314.
54. Sepúlveda, N., L. Petitjean, …, V. Hakim. 2013. Collective cell motion in an epithelial sheet can Be quantitatively described by a stochastic interacting particle model. *PLoS Comput. Biol.* 9:e1002944.
55. Brückner, D. B., N. Arlt, …, C. P. Broedersz. 2021. Learning the dynamics of cell–cell interactions in confined cell migration. *Proc. Natl. Acad. Sci. U S A.* 118:e2016602118.
56. Manova, R., T. A. van Beek, and H. Zuilhof. 2011. Surface functionalization by strain-promoted alkyne-azide click reactions. *Angew. Chem. Int. Ed. Engl.* 50:5428–5430.
57. Bubeník, J., M. Barešová, …, J. Donner. 1973. Established cell line of urinary bladder carcinoma (T24) containing tumour-specific antigen. *Int. J. Cancer.* 11:765–773.
58. Lang, K., B. Niggemann, …, F. Entschladen. 2002. Signal processing in migrating T24 human bladder carcinoma cells: role of the autocrine interleukin-8 loop. *Int. J. Cancer.* 99:673–680.
59. Jin, H., Y. Yu, …, C. Huang. 2015. Divergent behaviors and underlying mechanisms of cell migration and invasion in non-metastatic T24 and its metastatic derivative T24T bladder cancer cell lines. *Oncotarget.* 6:522–536.
60. Luo, K.-W., W.-Y. Lung, …, W.-R. Huang. 2018. EGCG inhibited bladder cancer T24 and 5637 cell proliferation and migration via PI3K/AKT pathway. *Oncotarget.* 9:12261–12272.
61. McBeth, L., A. C. Nwaneri, …, T. D. Hinds, Jr. 2016. Glucocorticoid receptor beta increases migration of human bladder cancer cells. *Oncotarget.* 7:27313–27324.
62. Hakim, V., and P. Silberzan. 2017. Collective cell migration: a physics perspective. *Rep. Prog. Phys.* 80:076601.
63. Petitjean, L., M. Reffay, …, P. Silberzan. 2010. Velocity fields in a collectively migrating epithelium. *Biophys. J.* 98:1790–1800.
64. Yamaguchi, N., T. Mizutani, …, H. Haga. 2015. Leader cells regulate collective cell migration via Rac activation in the downstream signaling of integrin β1 and PI3K. *Sci. Rep.* 5:7656.
65. Petrie, R. J., and K. M. Yamada. 2012. At the leading edge of three-dimensional cell migration. *J. Cell Sci.* 125:5917–5926.
66. Theveneau, E., and C. Linker. 2017. Leaders in collective migration: are front cells really endowed with a particular set of skills? *F1000Research.* 6:1899.
67. Brugués, A., E. Anon, …, X. Trepat. 2014. Forces driving epithelial wound healing. *Nat. Phys.* 10:683–690.

68. Qin, L., D. Yang, …, G. Xiao. 2021. Roles of leader and follower cells in collective cell migration. *Mol. Biol. Cell.* 32:1267–1272.
69. Zaritsky, A., D. Kaplan, …, I. Tsarfaty. 2014. Propagating waves of directionality and coordination orchestrate collective cell migration. *PLoS Comput. Biol.* 10:e1003747.
70. Farhadifar, R., J. C. Röper, …, F. Jülicher. 2007. The influence of cell mechanics, cell-cell interactions, and proliferation on epithelial packing. *Curr. Biol.* 17:2095–2104.
71. Serra-Picamal, X., V. Conte, …, X. Trepat. 2012. Mechanical waves during tissue expansion. *Nat. Phys.* 8:628–634.
72. Sarkar, D., G. Gompper, and J. Elgeti. 2021. A minimal model for structure, dynamics, and tension of monolayered cell colonies. *Commun. Phys.* 4:36.
73. Tarle, V., A. Ravasio, …, N. S. Gov. 2015. Modeling the finger instability in an expanding cell monolayer. *Integr. Biol.* 7:1218–1227.
74. Cates, M. E., and J. Tailleur. 2013. When are active Brownian particles and run-and-tumble particles equivalent? Consequences for motility-induced phase separation. *Europhys. Lett.* 101:20010.
75. Cooper, G. M. 2000, Sinauer Associates, Sunderland, MA. Cell-cell interactions. *In* The Cell: A Molecular Approach.
76. Nieman, M. T., R. S. Prudoff, …, M. J. Wheelock. 1999. N-cadherin promotes motility in human breast cancer cells regardless of their E-cadherin expression. *J. Cell Biol.* 147:631–644.
77. Kuphal, S., and A. K. Bosserhoff. 2006. Influence of the cytoplasmic domain of E-cadherin on endogenous N-cadherin expression in malignant melanoma. *Oncogene.* 25:248–259.
78. Reckamp, K. L., B. K. Gardner, …, S. M. Dubinett. 2008. Tumor response to combination celecoxib and erlotinib therapy in non-small cell lung cancer is associated with a low baseline matrix metalloproteinase-9 and a decline in serum-soluble E-cadherin. *J. Thorac. Oncol.* 3:117–124.
79. Oh, D. Y., K. W. Lee, …, Y. J. Bang. 2016. Phase II trial of dacomitinib in patients with HER2-positive gastric cancer. *Gastric Cancer.* 19:1095–1103.
80. Bodnar, L., R. Stec, …, C. Szczylik. 2018. Role of WNT/β-Catenin pathway as potential prognostic and predictive factors in renal cell cancer patients treated with everolimus in the second and subsequent lines. *Clin. Genitourin.Cancer.* 16:257–265.
81. Kuefer, R., M. D. Hofer, …, M. L. Day. 2003. The role of an 80 kDa fragment of E-cadherin in the metastatic progression of prostate cancer. *Clin. Cancer Res.* 9:6447–6452.
82. Schmeiser, K., and R. J. Grand. 1999. The fate of E- and P-cadherin during the early stages of apoptosis. *Cell Death Differ.* 6:377–386.
83. Trillsch, F., S. Kuerti, …, S. Mahner. 2016. E-Cadherin fragments as potential mediators for peritoneal metastasis in advanced epithelial ovarian cancer. *Br. J. Cancer.* 114:213–220.
84. Tang, M. K. S., P. Y. K. Yue, …, A. S. T. Wong. 2018. Soluble E-cadherin promotes tumor angiogenesis and localizes to exosome surface. *Nat. Commun.* 9:2270.
85. Grabowska, M. M., and M. L. Day. 2012. Soluble E-cadherin: more than a symptom of disease. *Front. Biosci. (Landmark Ed.).* 17:1948–1964.
86. Mialhe, A., G. Levacher, …, D. Seigneurin. 2000. Expression of E-, P-, n-cadherins and catenins in human bladder carcinoma cell lines. *J. Urol.* 164:826–835.
87. Theveneau, E., and R. Mayor. 2010. Integrating chemotaxis and contact-inhibition during collective cell migration: small GTPases at work. *Small GTPases.* 1:113–117.
88. Vedula, S. R. K., M. C. Leong, …, B. Ladoux. 2012. Emerging modes of collective cell migration induced by geometrical constraints. *Proc. Natl. Acad. Sci. U S A.* 109:12974.
89. Käfer, J., T. Hayashi, …, F. Graner. 2007. Cell adhesion and cortex contractility determine cell patterning in the *Drosophila* retina. *Proc. Natl. Acad. Sci. U S A.* 104:18549.
90. Hayashi, T., and R. W. Carthew. 2004. Surface mechanics mediate pattern formation in the developing retina. *Nature.* 431:647–652.
91. Chen, W. C., and B. Obrink. 1991. Cell-cell contacts mediated by E-cadherin (uvomorulin) restrict invasive behavior of L-cells. *J. Cell Biol.* 114:319–327.
92. Ayollo, D. V., I. Y. Zhitnyak, …, N. A. Gloushankova. 2009. Rearrangements of the actin cytoskeleton and E-cadherin-based adherens junctions caused by neoplasic transformation change cell-cell interactions. *PLoS One.* 4:e8027.
93. Huttenlocher, A., M. Lakonishok, …, A. F. Horwitz. 1998. Integrin and cadherin synergy regulates contact inhibition of migration and motile activity. *J. Cell Biol.* 141:515–526.
94. Bracke, M. E., H. Depypere, …, M. M. Mareel. 1997. Functional downregulation of the E-cadherin/catenin complex leads to loss of contact inhibition of motility and of mitochondrial activity, but not of growth in confluent epithelial cell cultures. *Eur. J. Cell Biol.* 74:342–349.
95. Theveneau, E., B. Steventon, …, R. Mayor. 2013. Chase-and-run between adjacent cell populations promotes directional collective migration. *Nat. Cell Biol.* 15:763–772.
96. Tanaka, M., S. Kuriyama, and N. Aiba. 2012. Nm23-H1 regulates contact inhibition of locomotion, which is affected by ephrin-B1. *J. Cell Sci.* 125:4343–4353.
97. Scarpa, E., A. Szabó, …, R. Mayor. 2015. Cadherin switch during EMT in neural crest cells leads to contact inhibition of locomotion via repolarization of forces. *Dev. Cell.* 34:421–434.
98. Wrighton, K. H. 2015. Cell migration: EMT promotes contact inhibition of locomotion. *Nat. Rev. Mol. Cell Biol.* 16:518.
99. Milano, D. F., N. A. Ngai, …, A. R. Asthagiri. 2016. Regulators of metastasis modulate the migratory response to cell contact under spatial confinement. *Biophys. J.* 110:1886–1895.
100. Sommers, C. L., E. W. Thompson, …, S. W. Byers. 1991. Cell adhesion molecule uvomorulin expression in human breast cancer cell lines: relationship to morphology and invasive capacities. *Cell Growth Differ.* 2:365–372.
101. Dietrich, M., H. Le Roy, …, C. P. Broedersz. 2018. Guiding 3D cell migration in deformed synthetic hydrogel microstructures. *Soft Matter.* 14:2816–2826.
102. Reinhart-King, C. A., M. Dembo, and D. A. Hammer. 2008. Cell-cell mechanical communication through compliant substrates. *Biophys. J.* 95:6044–6051.
103. Humphries, D. L., J. A. Grogan, and E. A. Gaffney. 2017. Mechanical cell–cell communication in fibrous networks: the importance of network geometry. *Bull. Math. Biol.* 79:498–524.
104. Majumdar, R., M. Sixt, and C. A. Parent. 2014. New paradigms in the establishment and maintenance of gradients during directed cell migration. *Curr. Opin. Cell Biol.* 30:33–40.
105. Camley, B. A. 2018. Collective gradient sensing and chemotaxis: modeling and recent developments. *J. Phys. Condens Matter.* 30:223001.